

This work was written as part of one of the author's official duties as an Employee of the United States Government and is therefore a work of the United States Government. In accordance with 17 U.S.C. 105, no copyright protection is available for such works under U.S. Law.

Public Domain Mark 1.0

<https://creativecommons.org/publicdomain/mark/1.0/>

Access to this work was provided by the University of Maryland, Baltimore County (UMBC) ScholarWorks@UMBC digital repository on the Maryland Shared Open Access (MD-SOAR) platform.

Please provide feedback

Please support the ScholarWorks@UMBC repository by emailing scholarworks-group@umbc.edu and telling us what having access to this work means to you and why it's important to you. Thank you.



Science Goals and Mission Concept for a Landed Investigation of Mercury

Carolyn M. Ernst¹ , Nancy L. Chabot¹ , Rachel L. Klima¹ , Sanae Kubota¹, Gabe Rogers¹, Paul K. Byrne^{2,3} , Steven A. Hauck, II⁴ , Kathleen E. Vander Kaaden⁵ , Ronald J. Vervack, Jr.¹ , Sébastien Besse⁶ , David T. Blewett¹ , Brett W. Denevi¹ , Sander Goossens^{7,8} , Stephen J. Indyk⁹, Noam R. Izenberg¹ , Catherine L. Johnson^{10,11} , Lauren M. Jozwiak¹, Haje Korth¹ , Ralph L. McNutt, Jr.¹ , Scott L. Murchie¹, Patrick N. Peplowski¹ , Jim M. Raines¹² , Elizabeth B. Rampe¹³ , Michelle S. Thompson¹⁴, and Shoshana Z. Weider¹⁵ 

¹ Johns Hopkins University Applied Physics Laboratory, Laurel, MD 20723, USA; carolyn.ernst@jhuapl.edu

² North Carolina State University, Raleigh, NC 27695, USA

³ Washington University in St. Louis, St. Louis, MO 63130, USA

⁴ Case Western Reserve University, Cleveland, OH 44106, USA

⁵ Jacobs, NASA Johnson Space Center, Mail Code XI3, Houston, TX 77058, USA

⁶ Aurora Technology BV for ESA, European Space Agency, Madrid, Spain

⁷ University of Maryland Baltimore County, Baltimore, MD 21250, USA

⁸ NASA Goddard Space Flight Center, Greenbelt, MD 20771, USA

⁹ Honeybee Robotics, Altadena, CA 91001, USA

¹⁰ University of British Columbia, Vancouver, BC V6T 1Z4, Canada

¹¹ Planetary Science Institute, Tucson, AZ 85719, USA

¹² University of Michigan, Ann Arbor, MI 48109, USA

¹³ NASA Johnson Space Center, Houston, TX 77058, USA

¹⁴ Purdue University, West Lafayette, IN 47907, USA

¹⁵ Agile Decision Sciences, Beltsville, MD 20705, USA

Received 2020 November 16; revised 2021 August 6; accepted 2021 August 6; published 2022 March 25

Abstract

Mercury holds valuable clues to the distribution of elements at the birth of the solar system and how planets form and evolve in close proximity to their host stars. This Mercury Lander mission concept returns in situ measurements that address fundamental science questions raised by the MErcury Surface, Space ENvironment, GEochemistry, and Ranging (MESSENGER) mission's pioneering exploration of Mercury. Such measurements are needed to understand Mercury's unique mineralogy and geochemistry, characterize the proportionally massive core's structure, measure the planet's active and ancient magnetic fields at the surface, investigate the processes that alter the surface and produce the exosphere, and provide ground truth for remote data sets. The mission concept achieves one full Mercury year (~88 Earth days) of surface operations with an 11-instrument, high-heritage payload delivered to a landing site within Mercury's widely distributed low-reflectance material, and it addresses science goals encompassing geochemistry, geophysics, the Mercury space environment, and geology. The spacecraft launches in 2035, and the four-stage flight system uses a solar electric propulsion cruise stage to reach Mercury in 2045. Landing is at dusk to meet thermal requirements, permitting ~30 hr of sunlight for initial observations. The radioisotope-powered lander continues operations through the Mercury night. Direct-to-Earth communication is possible for the initial 3 weeks of landed operations, drops out for 6 weeks, and resumes for the final month. Thermal conditions exceed lander operating temperatures shortly after sunrise, ending operations. Approximately 11 GB of data are returned to Earth. The cost estimate demonstrates that a Mercury Lander mission is feasible and compelling as a New Frontiers-class mission.

Unified Astronomy Thesaurus concepts: [Mercury \(planet\) \(1024\)](#); [Landers \(901\)](#); [Surface composition \(2115\)](#); [Planetary interior \(1248\)](#); [Planetary magnetosphere \(997\)](#); [Exosphere \(499\)](#); [Surface processes \(2116\)](#)

1. Introduction

Mariner 10 provided our first close-up reconnaissance of Mercury. Although the spacecraft imaged less than half of the surface during its three flybys in 1974–1975, those images revealed a heavily bombarded surface, suggestions of widespread volcanism, and evidence for global contraction (Murray et al. 1974, 1975). Mariner 10 magnetometer data indicated the presence of a global magnetic field (Ness et al. 1974, 1975), a surprising result given the expectation, at the time, that the iron core of the small planet would have long since frozen (Solomon 1976; Schubert et al. 1988). Observations by Mariner

10 led to the discovery of the planet's thin exosphere, as seen in emission from H, He, and possibly O (Broadfoot et al. 1976).

The MErcury Surface, Space ENvironment, GEochemistry, and Ranging (MESSENGER) spacecraft performed three flybys of Mercury in 2008 and 2009, before entering orbit in 2011. MESSENGER's four-year orbital investigation enabled numerous discoveries, several of which led to substantial or complete changes in our fundamental understanding of the planet: the widespread presence of volatile elements such as Na, K, and S (Nittler et al. 2011; Peplowski et al. 2011; Evans et al. 2012); a surface with extremely low iron abundance (Nittler et al. 2011; Evans et al. 2012; Weider et al. 2014), whose darkening agent is likely carbon (Murchie et al. 2015; Peplowski et al. 2016; Klima et al. 2018); a previously unknown karst-like planetary landform—hollows—that may form by volatile sublimation from within rocks exposed to the harsh conditions on the surface



Original content from this work may be used under the terms of the [Creative Commons Attribution 4.0 licence](#). Any further distribution of this work must maintain attribution to the author(s) and the title of the work, journal citation and DOI.

(Blewett et al. 2011, 2016); expansive volcanic plains (Head et al. 2011) and pyroclastic vents (Kerber et al. 2011) that have shaped Mercury’s geology through time; much more radial contraction of the planet than previously thought (Byrne et al. 2014); an offset of the magnetic equator from that of the planet (Anderson et al. 2011); crustal magnetization indicating an ancient magnetic field (Johnson et al. 2015, 2018); unexpected seasonal variability and relationships among exospheric species and processes that generate them (Burger et al. 2014; Cassidy et al. 2015, 2016; Vervack et al. 2016; Merkel et al. 2017, 2018); an extreme space environment driven by the solar wind (Slavin et al. 2008, 2009, 2014) with unexpectedly energetic heavy planetary ions (Zurbuchen et al. 2008, 2011; Raines et al. 2013, 2014); the presence in the permanently shadowed polar terrain of water ice and other volatile materials likely to include complex organic compounds (Lawrence et al. 2013; Neumann et al. 2013; Paige et al. 2013; Chabot et al. 2018); and a definitive determination of Mercury’s large molten core (Margot et al. 2012; Hauck et al. 2013; Rivoldini & Van Hoolst 2013), as well as evidence for the existence of a solid inner core (Genova et al. 2019). Additionally, Earth-based telescopic observations provide a long-term baseline of exosphere and surface observations extending across spacecraft visits, covering Mariner 10 to MESSENGER and continuing into the future (e.g., Sprague et al. 2000; Mendillo et al. 2001; Bida & Killen 2017).

MESSENGER revolutionized our understanding of Mercury, and the dual-spacecraft ESA–JAXA BepiColombo mission (Benkhoff et al. 2010, 2021) promises further revelations in Mercury science. BepiColombo launched in 2018 and will fly by Mercury six times before Mercury orbital insertion in late 2025. The mission consists of two complementary spacecraft: the Mercury Magnetospheric Orbiter (“Mio,” formerly MMO; Murakami et al. 2020) and the Mercury Planetary Orbiter (MPO). Mio will be in a 590 km × 11,640 km polar orbit with a period of 9.3 hr, whereas MPO will be in a 480 km × 1500 km polar orbit with a period of 2.3 hr. Nominal science operations will last for one Earth year, followed by a planned extension of another year.

Despite the profound discoveries they have enabled, remote and orbital investigations have technical limits. Landed, in situ measurements from Mercury’s surface are needed to address several fundamental science questions. In particular, MESSENGER revealed that Mercury’s highly chemically reduced and unexpectedly volatile-rich composition is unique among terrestrial planets and unlike any predictions of previously proposed hypotheses of the planet’s origin. These surprising results have led to a reexamination of the planet’s formation and history. In situ measurements from the surface are needed to (1) understand Mercury’s unique mineralogy and geochemistry, (2) characterize the proportionally massive core’s structure, (3) measure the planet’s active and ancient magnetic fields at the surface, (4) investigate the processes that alter the surface and produce the exosphere, and (5) provide ground truth for current and future remote data sets. Although BepiColombo will further advance our global understanding of Mercury, that mission cannot address the major science questions for which in situ landed measurements are needed, nor will it image Mercury’s surface with sufficient resolution (Flamini et al. 2010; Cremonese et al. 2020) to influence the technical approach used to land.

Additionally, unraveling the mysteries of Mercury’s origin, evolution, and ongoing processes has implications and

expected significance beyond the innermost planet. Mercury is an extreme end-member of planet formation, and its highly reduced nature provides clues to how planets close to their host stars can form and evolve. Mercury’s magnetosphere is also a natural laboratory for understanding the interactions of exoplanets with their host stars. The acquisition and retention of crustal magnetizations over billion-year timescales has implications for dynamo generation across the major terrestrial bodies. Understanding the processes that affect the regolith of airless bodies provides key insight into exospheres and space weathering on bodies within the solar system and beyond. A Mercury lander would accomplish groundbreaking science, and the results would inform our greater understanding of the formation and evolution of rocky planets in the solar system and dense, metal-rich planets around other stars (e.g., Barclay et al. 2013).

In preparation for the 2023–2032 Planetary Science and Astrobiology Decadal Survey by the National Academies of Sciences, Engineering, and Medicine, NASA funded a high-fidelity mission concept study to evaluate the science, technical feasibility, and cost associated with conducting a landed mission to Mercury. In this paper, we detail the science motivation for such a future mission and the science implementation of the NASA-funded mission concept study. Additional technical details can be found in the report delivered to NASA (Ernst et al. 2020).

2. Background

The importance of a landed mission to Mercury was recognized by the 2013–2022 Decadal Survey (National Research Council 2011), and a previous Mercury Lander Mission Concept Study (Hauck et al. 2010) was completed in response that examined the feasibility of a Mercury lander. The 2010 Concept Maturity Level 3 (CML-3) (trade space) Mercury Lander Study was conducted prior to MESSENGER’s orbital campaign, however, and the study was unable to incorporate MESSENGER’s orbital results to inform the science justification for landed in situ measurements. Since that time, MESSENGER’s data sets have transformed our understanding of Mercury, greatly advancing the scientific case for a landed mission. The degree of scientific thought and consideration brought to bear on this study’s lander payload and scientific measurements is a major distinguishing factor from the 2010 study.

Further, the technology landscape has changed substantially in the past decade, with new launch vehicle (LV) availability and increased development and use of solar electric propulsion (SEP) systems. Both are enabling contributions to this design concept and address the two areas that the 2010 study report recognized as particularly challenging: the impacts of launch energy and velocity change (ΔV) requirements. In addition, costing guidelines for NASA’s New Frontiers missions have changed since 2010. The previous study concluded that the cost of such a mission exceeded the cost cap of a PI-led New Frontiers-class mission. However, LV and Phase E–F mission operation costs have been excluded from the cost cap in the most recent New Frontiers mission selection. Consequently, the costing associated with this new mission concept enables an informed discussion for the 2023 Decadal Survey based on the latest science results and technology capabilities.

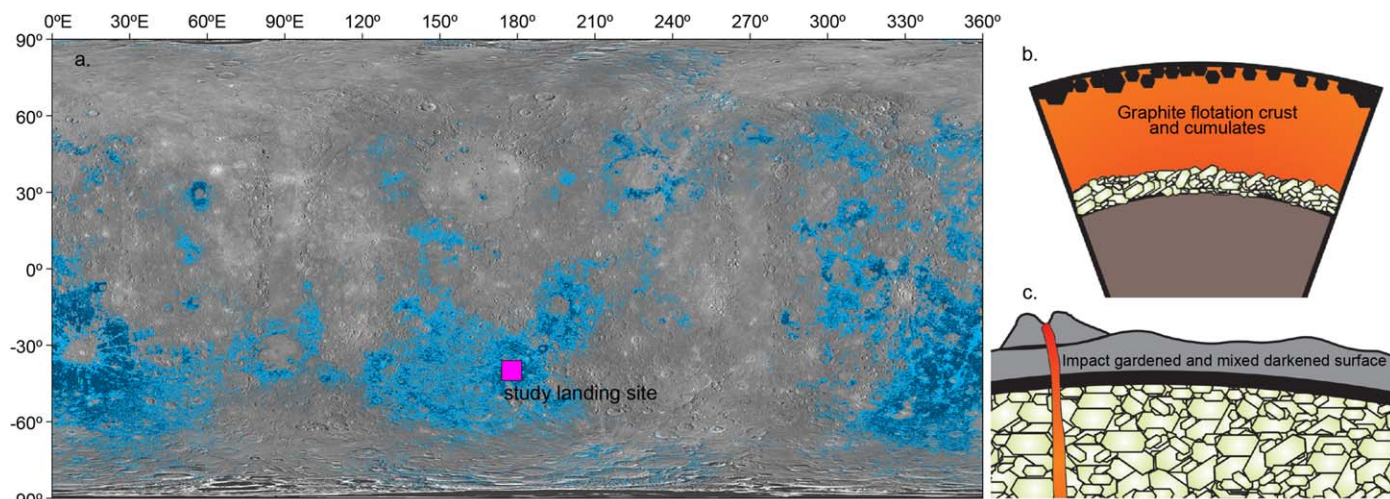


Figure 1. (a) Mercury’s globally distributed LRM (shown in blue; Klima et al. 2018), which may include ancient, carbon-bearing deposits. The pink square denotes the landing site location (40°S, 178°E) considered for this mission concept study. (b) A thin, primary graphite flotation crust forms in an early magma ocean. (c) Impacts mix the volcanic secondary crust and the graphite primary crust (panels (b) and (c) from Vander Kaaden et al. 2019).

3. Mercury Lander Science Goals

To inform the Mercury Lander mission concept study, four overarching and fundamental science goals were identified:

Goal 1: Investigate the highly chemically reduced, unexpectedly volatile-rich mineralogy and chemistry of Mercury’s surface, to understand the earliest evolution of this end-member of rocky planet formation.

Goal 2: Investigate Mercury’s interior structure and magnetic field, to unravel the planet’s differentiation and evolutionary history and to understand the magnetic field at the surface.

Goal 3: Investigate the active processes that produce Mercury’s exosphere and alter its regolith, to understand planetary processes on rocky airless bodies, including the Moon.

Goal 4: Characterize the landing site, to understand the processes that have shaped its evolution, to place in situ measurements in context, and to enable ground truth for global interpretations of Mercury.

To evaluate the technical feasibility of a landed mission to Mercury fully, including the mission design aspects, it is necessary to select a specific landing site on the planet. A landing site in the low-reflectance material (LRM) was chosen for this study. MESSENGER results showed up to 4 wt% enrichment in carbon over the local mean in the LRM excavated from depth, and as much as 2.5 wt% enrichment in carbon in other regional LRM deposits associated with the planet’s most heavily cratered terrains (Peplowski et al. 2016; Klima et al. 2018). The LRM is postulated to contain remnants of Mercury’s “exotic” graphite flotation crust (Vander Kaaden & McCubbin 2015) and, hence, may represent the earliest solid crustal materials on Mercury, providing a unique window into the planet’s earliest differentiation. Additionally, LRM locations are widely distributed across the planet (Figure 1), providing flexibility for the mission concept study—without being overly limited by, or prescriptive of, a specific choice of landing site.

This choice of landing site, however, should not restrict future landed exploration of Mercury. There are compelling scientific cases to be made for a wide range of landing locations, such as the diverse geochemical units on Mercury,

including the northern smooth plains and the “high-Mg region” (e.g., Peplowski et al. 2015; Weider et al. 2015; Nittler et al. 2020); geologically younger pyroclastic vents (Thomas et al. 2015); the enigmatic hollows (Blewett et al. 2013, 2016); and the ice-rich, permanently shadowed polar deposits (Chabot et al. 2018). The overarching science goals remain the same regardless of the ultimate landing site choice, although the specifics of some science objectives and measurements would be adapted, such as for Goal 1 for a landing in a polar deposit. Nonetheless, the measurements made by the first landed mission to Mercury will be foundational and transformative, answering high-priority outstanding science questions for Mercury regardless of the selected landing location.

The following sections detail the scientific motivation driving each of these goals. We title each investigation in shorthand terms that correspond to the broad topics they encompass, i.e., geochemistry, geophysics, space environment, and geology. We emphasize, however, that many aspects of our science goals, and the instruments we describe to address those goals, are cross-cutting, and these terms are therefore neither exhaustive nor exclusive to each goal.

3.1. Goal 1: Geochemistry

Pre-MESSENGER hypotheses for Mercury’s origin and extremely large core predicted a variety of silicate compositions for the planet’s present makeup, and MESSENGER’s compositional measurements were planned to distinguish definitively these competing ideas (Solomon et al. 2001). MESSENGER orbital measurements from the Gamma-Ray, Neutron, and X-ray Spectrometers (GRS, NS, XRS, respectively) indicated, however, that Mercury’s surface is enriched in moderately volatile elements such as K and Na, has high S (up to 4 wt%) and low Fe contents (less than 1–2 wt%), and is rich in C (up to 5 wt%) (Nittler et al. 2011, 2018; Peplowski et al. 2011, 2012, 2016; Evans et al. 2015; Weider et al. 2015, 2016; Klima et al. 2018). These measurements revealed that Mercury’s surface composition could not be fully explained by predictions from previously proposed formation hypotheses, which include a giant impact scenario, evaporation models, and direct formation from high-temperature nebular condensates (e.g., Ebel & Stewart 2018). These surprising

results have led to a complete reexamination of the planet's origin and history. Mercury's unique geochemical signatures revealed by MESSENGER are indicative of highly reduced conditions during planetary formation and differentiation (McCubbin et al. 2012; Zolotov et al. 2013; Namur et al. 2016). The surface composition of Mercury is modeled as Mg-rich silicates (e.g., forsterite, enstatite), oxides, exotic sulfides (e.g., niningerite, oldhamite), and metals (Stockstill-Cahill et al. 2012; Vander Kaaden & McCubbin 2016; Namur & Charlier 2017). However, owing to the lack of strong spectral features at ultraviolet, visible, and near-infrared wavelengths, it was not possible with MESSENGER to make direct assessments of Mercury's surface mineralogy.

Nevertheless, the measured elemental chemistry and inferred highly reduced conditions have led to new hypotheses for the formation of Mercury that differ from those of all other bodies in the solar system (e.g., Ebel & Stewart 2018). In particular, the high C content on the surface has been proposed to reflect a primary graphite flotation crust (Figure 1; see also Vander Kaaden & McCubbin 2015). Remnants of this exotic graphite flotation crust would represent the earliest solid crustal materials on Mercury, providing a window into the planet's differentiation. After the magma ocean solidified, volcanic eruptions resurfaced the majority of the planet, covering and entraining that graphite crust (e.g., Denevi et al. 2018b). Impacts have since excavated and mixed the graphite with the surface material (e.g., Rivera-Valentin & Barr 2014). Remnants of the graphite crust are inferred to be concentrated in the LRM exposures, distributed across the surface of Mercury. As materials erupted through this C-rich layer, the melts are hypothesized to have been stripped of their oxygen, producing CO that was lost to space (e.g., through pyroclastic vents; Kerber et al. 2009; Weider et al. 2016), and resulting in smelting reactions leaving highly reduced metals (e.g., Si-rich metals) on the surface (McCubbin et al. 2017).

Mercury's surface mineralogy is thus hypothesized to be unlike that of any other solar system terrestrial body, making Mercury the most highly reduced end-member of the terrestrial planets, and suggesting a unique environment for planetary differentiation and subsequent evolution. Although MESSENGER's compositional data acquired from orbit called into question previous models of the planet's formation and evolution, only in situ geochemical measurements will enable us to test new hypotheses. BepiColombo is positioned to add to our compositional knowledge (Rothery et al. 2020), in particular by improving coverage of elemental compositional measurements over the southern hemisphere and better characterizing silicate mineralogy using orbital thermal infrared imaging spectroscopy (e.g., Hiesinger et al. 2020). Yet, direct in situ elemental and mineralogical measurements on Mercury's surface are essential to address the new science questions that have arisen since MESSENGER.

One crucial measurement for a landed mission to Mercury would be of the major and minor elemental compositions of the LRM, at a spatial scale and sensitivity far superior to orbital measurements that were taken by MESSENGER or will be acquired by BepiColombo. In particular, quantifying the LRM's C content, volatile-element abundances (e.g., Na, K, S), and minor elements that are not well resolved from orbit (e.g., Cl, Cr, and Mn) will enable current hypotheses regarding LRM to be tested and provide key constraints to advance petrologic modeling (e.g., Stockstill-Cahill et al. 2012; Vander Kaaden

et al. 2017) and laboratory experimental studies (e.g., Charlier et al. 2013; Namur et al. 2016; Vander Kaaden & McCubbin 2016). Elemental measurements from the surface of Mercury could also be related directly to MESSENGER and BepiColombo orbital measurements, to place the landed data in a global context.

The most critical information to be obtained by a Mercury lander from a geochemical standpoint, however, is the mineralogical hosts of the measured elements. Understanding the mineralogy of Mercury's exotic surface materials opens a window into the thermochemical evolution of the planet that is currently closed. Characterizing Mercury's mineralogy and quantifying the phases present at the 1-wt% level are necessary to interpret the petrologic history, oxidation states, and early processes the planet experienced. Understanding the mineralogical host(s) of Mercury's surprisingly high content of surface-bound S will provide key insights into the planet's differentiation and evolutionary history and help to determine the phase that, upon removal, forms Mercury's mysterious hollows—which are closely associated spatially with the LRM (e.g., Blewett et al. 2011; Thomas et al. 2014). Mineralogical measurements acquired from the surface of Mercury will revolutionize our view of the planet, enable the next step in understanding its formation, and advance our understanding of planetary evolution under highly reducing conditions more broadly. Evaluating any heterogeneity at the landing site by acquiring compositional and mineralogical measurements from multiple locations could provide additional information about the geologic evolution of the planet.

Key Goal 1 Questions:

1. What is the composition of the LRM on Mercury, and what does this tell us about the primary processes taking place on the planet?
2. What role does C play in controlling the development of space weathering features on airless surfaces?
3. What do the volatile abundances of Mercury tell us about volatile distribution across the inner solar system?
4. Is the LRM the planet's primary crust, and if so, how does the composition of Mercury's primary crust compare with the primary crusts of other planetary bodies?
5. How can the data from MESSENGER and BepiColombo be refined with new ground-truth data?

3.2. Goal 2: Geophysics

Mercury's high bulk density is a critical indicator of the planet's origin and subsequent evolution (e.g., Siegfried & Solomon 1974; Schubert et al. 1988; Benz et al. 2007; Brown & Elkins-Tanton 2009; Ebel & Stewart 2018; Hauck et al. 2018; Margot et al. 2018). Accurate determination of the interior structure of Mercury is essential for characterizing the bulk composition of the planet—because each major layer (e.g., crust, mantle, and liquid and solid portions of the core) has a different composition (Nittler et al. 2018)—as well as for understanding the conditions of its long-term evolution. The internal configuration of Mercury is an indicator of how the planet formed and differentiated, and that same structure sets the boundary conditions for how Mercury has evolved. MESSENGER confirmed the existence of a liquid portion of the metallic core and substantially improved our knowledge of the layering of the interior (e.g., Smith et al. 2012; Hauck et al. 2013; Rivoldini &

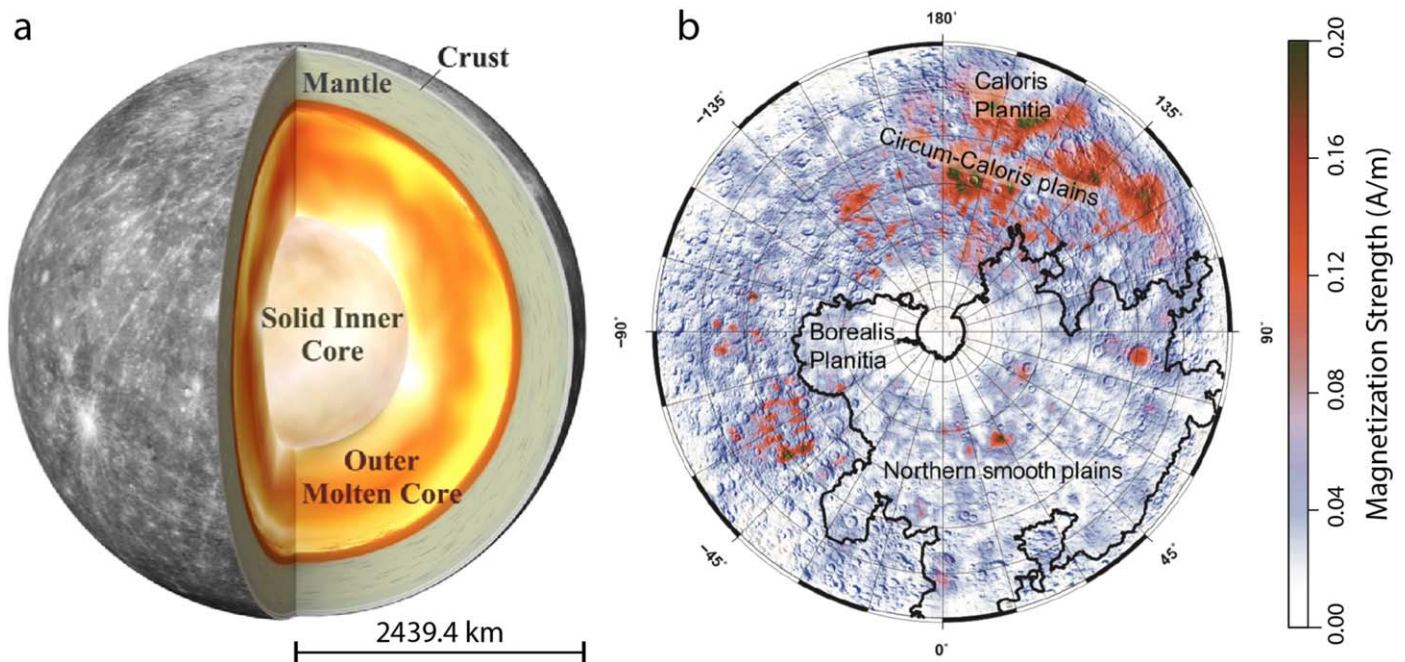


Figure 2. (a) Mercury's interior structure (from Genova et al. 2019). (b) Crustal magnetization strength for Mercury's northern hemisphere assuming a 10-km thick magnetized layer (from 30°N to the pole). The magnetization comprises both ancient and modern contributions, the latter induced by the present field (after Hauck & Johnson 2019). In situ measurements will determine interior structure and directly measure magnetic fields at the surface.

Van Hoolst 2013; Margot et al. 2018; Genova et al. 2019; see Figure 2). Analysis of early MESSENGER data led to the consideration of a solid iron sulfide layer at the top of the core, but further analysis of the full MESSENGER data sets no longer favors the existence of such a layer (Hauck et al. 2018; Margot et al. 2018). However, greater accuracy in determining the thicknesses and densities of these layers, including the solid inner core, is critical for understanding the history of magnetic field generation and global contraction (e.g., Siegfried & Solomon 1974; Schubert et al. 1988; Hauck et al. 2004, 2018; Christensen 2006; Tosi et al. 2013; Cao et al. 2014; Tian et al. 2015; Johnson et al. 2018).

Mercury's rotational dynamics (e.g., libration and obliquity) are sensitive to the interior structure, as well as internal couplings and external forcings, e.g., from internal gravitational coupling among component layers versus perturbations from Jupiter (e.g., Peale 2005; Margot et al. 2012, 2018; Stark et al. 2015). Documenting these internal and external influences is critical for ascertaining Mercury's internal structure, especially the properties of the core (e.g., Dumberry 2011; Veasey & Dumberry 2011; Van Hoolst et al. 2012; Dumberry et al. 2013; Koning & Dumberry 2013; Genova et al. 2019). Direct-to-Earth radio tracking from a stationary lander position over time provides more accurate information regarding the rotation of the surface than can be derived from orbital data, by avoiding ambiguities due to spacecraft motion, orbit errors, and aliasing. Currently, analyses based on either gravity (Genova et al. 2019) or altimetry (e.g., Stark et al. 2015) and Earth-based radar data (e.g., Margot et al. 2012) yield statistically distinct results for Mercury's average spin rate. Landed measurements will resolve this discrepancy because they will be a fully independent data set and approach, which also offer a greater number of precise measurements over a substantial portion of a rotation period than Earth-based or orbital data can provide. Further, these data will also extend the temporal baseline of observations beyond MESSENGER and BepiColombo that

will be crucial to determine accurately the long-period effects on physical librations, including those forced by Jupiter on timescales of its orbital period around the Sun. Such knowledge is necessary to separate components of the rotational state and so determine the planet's internal structure.

The internal evolution and geological evolution of a planet are driven by how heat is generated, transferred from the interior to the surface, and lost to space. The current thermal state of the interior is an essential input for understanding its 4.5 Gyr of planetary evolution. Measurements of the tidal Love numbers (e.g., k_2) and phase lag from the tide-raising potential provide constraints on Mercury's interior layering and how the crust and mantle deform viscoelastically on tidal periods (e.g., Padovan et al. 2014; Steinbrügge et al. 2018). MESSENGER measurements of k_2 , based on orbital gravity data, will be supplemented by those of BepiColombo (e.g., Genova et al. 2021); however, direct measurements of the tidal changes in the gravity field at the surface are necessary to determine the rheological structure of the interior (Steinbrügge et al. 2018). Such measurements would enable the phase lag of the tidal response, which is sensitive to internal temperatures, to be characterized and would also provide a direct assessment of the solid-body tide. The important interrelationships among the density, thermal, and rheological structures of Mercury's interior afford an opportunity to characterize robustly the modern state of the interior and its evolution to the present.

Mercury's magnetic field provides a direct indicator of the dynamics of the interior both in the modern era (via the internal core field) and in the deep past (via remanent crustal magnetization of ancient terranes; e.g., Johnson et al. 2015, 2018; Hauck et al. 2018). The surface magnetic field strength is $\sim 1\%$ that of Earth, and the field is highly symmetric about the planet's rotation axis but has a magnetic equator that is offset ~ 480 km north from the geographic equator (Anderson et al. 2011). The pivotal discovery of the magnetization of ancient portions of Mercury's lithosphere

(Johnson et al. 2015) opened new lines of inquiry into how the magnetic field has operated and how the planet evolved (Hood 2016; Hauck et al. 2018; Johnson et al. 2018). MESSENGER measurements showed that much of the northern hemisphere has a weakly magnetized lithosphere, with some regions having locally much stronger magnetizations (Hood 2016; Johnson et al. 2018; see Figure 2).

Although the weak magnetizations could result from those induced in the present field, the strong magnetizations are most easily explained as remanent magnetization acquired in an ancient field (Johnson et al. 2015; Hauck & Johnson 2019). Furthermore, time-varying fields in Mercury's magnetosphere induce electrical currents in the interior and secondary magnetic fields. These induced fields, resolved with MESSENGER data, are a probe of interior electrical conductivity structure and have already provided a complementary constraint on the core radius from those offered by geodetic and rotational observations (Johnson et al. 2016; Wardinski et al. 2019; Katsura et al. 2021). Orbital mapping by MESSENGER (and, in time, BepiColombo) provides a global picture of these processes. However, small-amplitude crustal fields, as well as time-varying fields due to induction in Mercury's mantle, are difficult to detect from orbit because of the strong altitude-dependent decay of the signal. Measurements made on the surface substantially increase the ability to characterize the internal field, in particular crustal fields and time-varying fields induced in the interior. Indeed, measurements of ambient static fields >10 nT above the current models of the core field contribution of the surface would clearly establish crustal or mode localized core field contributions to the internal field. Induced fields could be measured by monitoring the slow variation of field strength from dusk to dawn.

Determining the mineral(s) that carry the crustal magnetization is a fundamental issue related to interior composition and is needed to place bounds on the relative contributions of magnetization induced in the present field and acquired in an ancient field. Understanding the relative contributions of both modern and ancient magnetization is important because the existence of an ancient field at 3.9–3.7 Ga, comparable to or up to 100 times stronger than the present field, places restrictive constraints on models of the thermal history of the core and thus of the interior and evolution of Mercury as a whole (Johnson et al. 2015, 2018; Hauck et al. 2018).

Key Goal 2 Questions:

1. How thick are each of the major layers (crust, mantle, outer core, and inner core) of Mercury's interior?
2. What is the current rate of seismic activity on Mercury?
3. What are the minerals that carry crustal magnetization on Mercury?
4. What is the modern thermal and rheological state of Mercury's interior?

3.3. Goal 3: Space Environment

Three primary sources generate exospheres and cause space weathering on airless bodies: solar radiation, charged particles, and micrometeoroids (Figure 3; e.g., Killen et al. 2018). Mercury—under intense solar radiation, with a highly dynamic magnetosphere, and subject to high-speed micrometeoroid bombardment—serves as an excellent laboratory for studying all three sources and the complex interactions among the various processes involved (e.g., Domingue et al. 2014). As

these phenomena affect Mercury's surface, they release neutral atoms and molecules, as well as ions, into the exosphere. MESSENGER measured (and BepiColombo will measure; Milillo et al. 2020) these from orbit in two ways: remotely and locally in situ. Orbital remote sensing measurements of emission from the released species are generally averaged over thousands of kilometers (e.g., Burger et al. 2014; Merkel et al. 2018). In situ point measurements of the exosphere made in orbit are more localized but cannot determine where the particles originated (e.g., Raines et al. 2013). Orbital observations therefore provide only an overall sense of the outputs of each process. Similarly, although the input flux of charged particles impinging on Mercury's surface has been estimated through orbital observations from MESSENGER (e.g., Raines et al. 2014; Winslow et al. 2014), there is still considerable ambiguity regarding these particles' contributions. Many factors that cannot be measured from orbit, such as unexpected magnetic field configurations and small-scale plasma processes, could substantially alter the flux and energy distribution of particles that actually reach the surface.

Our current understanding of the micrometeoroid (dust grain) influx at Mercury relies primarily on models (e.g., Christou et al. 2015). The majority of dust grains may also be charged (Mann et al. 2004) and thus subject to the same unknown factors that affect the flux of charged particles. Only in situ measurements from the surface can make the precise, small-scale measurements that connect all these pieces together into a complete picture of the processes at work on the surface of Mercury.

Landed observations on Mercury will enable the quantification of release processes in detail through concurrent, local-scale measurements of both neutrals and ions released from the surface, incident fluxes of charged particles and micrometeoroids, and detailed measurements of the surface mineralogy. These first observations from Mercury's surface will provide critical measurements for understanding highly localized processes; despite the limitations of fully addressing the complexity of such processes from a single landed position, measurements over a full Mercury orbit will enable investigations of seasonal and other time-varying fluctuations, which will be key as the first landed measurements to interpret these processes.

Furthermore, a lander that experiences both twilight and night conditions provides the opportunity to distinguish the direct effects of sunlight from those of charged particles and dust by observing trends in the inputs and outputs with time. Surface measurements are also necessary for addressing other factors, including relationships among incoming sunlight, charged particles, micrometeoroids, and the released neutral and ionized species; temporal variability of the incoming and outgoing fluxes; whether the stoichiometry of the surface minerals is reflected in the released material; how the fluxes inform both recycling to the surface and loss to space; and to what extent physical regolith parameters (e.g., binding energies) play a role in these interactions.

Equally integral to a complete understanding of how material is released from Mercury's surface are measurements of the surface itself. Solar-wind irradiation and micrometeoroid impacts contribute to space weathering of the surface, a phenomenon that occurs on all airless bodies. The effects of these processes on the microstructure, chemistry, and optical properties of material at Mercury are poorly understood

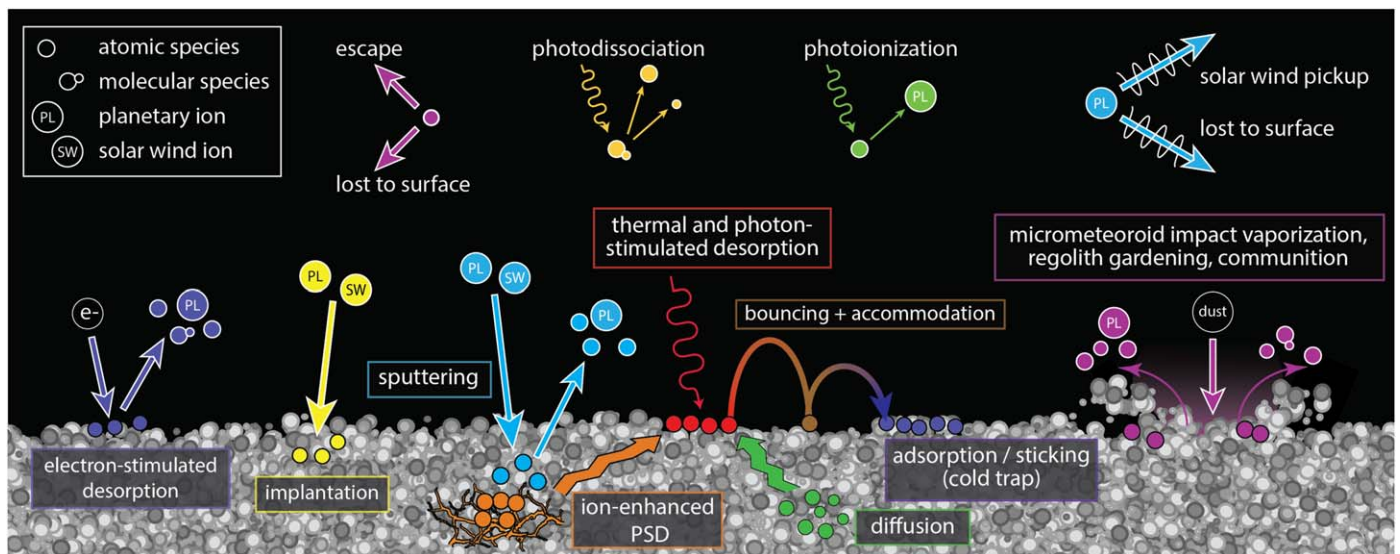


Figure 3. Schematic of the processes that act on Mercury's surface to generate and maintain the exosphere and contribute to space weathering of the regolith. Exospheric sources and space weathering processes are illustrated at the surface itself; intermediate and loss processes in the exosphere are illustrated at the top. In situ measurements from the surface will directly resolve the contributions of each process.

(e.g., Hapke 2001; Bennett et al. 2013; Pieters & Noble 2016). Beyond compositional (i.e., elemental and mineralogical) measurements, it is important to understand the physical parameters of the regolith (e.g., particle size, strength, porosity) that also affect how the release processes operate. In particular, the physical properties of the regolith dictate the depth to which electromagnetic radiation or charged particles can penetrate, controlling how quickly the products from these interactions can diffuse back to the surface and be released to the exosphere, and governing the rate at which gardening of the regolith brings fresher materials to the surface. Investigating the character of the regolith in the near subsurface, in color and at pixel scales $\leq 500 \mu\text{m}$ (to resolve millimeter-sized grains), would enable further understanding of space weathering on Mercury. Landed in situ regolith measurements can address key questions, including how the effects of the release processes change with the regolith's physical parameters, the nature of gardening on the surface, and the space weathering environment at Mercury.

Key Goal 3 Questions:

1. What are the composition, flux, and temporal variability of exospheric neutrals and charged particles (both incoming and outgoing) near the surface, and how are they correlated?
2. What is the flux of dust particles to the surface, and how does the release of exospheric material respond to variations in the dust flux?
3. How is the composition of the surface reflected in material released to the exosphere?
4. What is the space weathering environment at Mercury?
5. How does the unique geochemistry of the Mercury surface affect its space weathering characteristics?

3.4. Goal 4: Geology

Although some MESSENGER Mercury Dual Imaging System (MDIS) images resolved surface features as small as a few meters across (e.g., Blewett et al. 2018), the vast majority

of the surface was observed at much lower resolution (yielding global image mosaics at 166 m pixel^{-1} ; e.g., Denevi et al. 2018a). BepiColombo will provide important new images of the innermost planet (Rothery et al. 2020), acquiring global coverage at 50 m pixel^{-1} and local coverage ranging from $\sim 10 \text{ m pixel}^{-1}$ soon after beginning orbital operations to 2–3 m pixel^{-1} locally later in the mission (Flamini et al. 2010; Cremonese et al. 2020). But even with images with resolutions of several meters per pixel, there remains a gap between orbital observations and in situ, lander-scale observations that must be bridged to tie a landing site to our global framework for Mercury. Connecting observations from orbit to touchdown by acquiring nested images during descent, as well as tracking prominent landforms, would help to obtain positional data for the lander (e.g., Grotzinger et al. 2012). Nested descent images would also enable characterization of the site itself in the context of a continuum of scales across the descent sequence, such as the size–frequency distribution of boulders and craters and the visibility of different landforms at different scales. Such data would provide key information for placing the landing site in particular and inferences of Mercury's surface more generally into the context of orbital observations.

Mercury's local geological characteristics are currently unknown, particularly at outcrop scales. Yet vital insights have been gained by landers and rovers operating at that scale on other planetary bodies (e.g., Squyres et al. 2006; Smith et al. 2009; Eppes et al. 2015), affording us a view of planetary processes impossible to achieve from orbit (Figure 4). Imaging a substantial fraction of the lander surroundings ($\geq 180^\circ$ azimuth, with coverage from the horizon down to the near-field surface) with the ability to resolve 10-cm-sized features within 50 m of the lander will return invaluable geomorphological, textural, and structural information with which to ask key outstanding questions regarding the landscape itself (Bell et al. 2003; Grotzinger et al. 2012). Characterizing the landing site is necessary for identifying, for instance, local small-scale volcanic and tectonic features, as well as evidence for hollows at the LRM-rich landing site. Landed images will be used to determine local landing site regolith and rock heterogeneity,

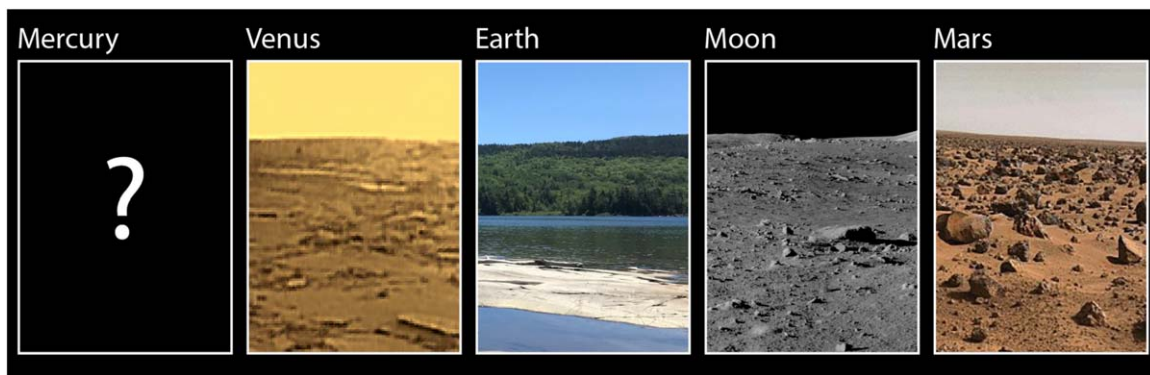


Figure 4. Mercury is the only major terrestrial body for which in situ surface data are lacking, yet the planet holds unique value in understanding how planets form and evolve.

and whether there is evidence for processes that have altered, and continue to alter, the surface. These images could reveal textures, landforms, etc., at the surface that have not been recognized from orbit.

Comprehensive assessment of the landing site will provide context with which to better understand global observations. Documenting the chemical composition of a landing site will provide “ground truth” for the compositional and geochemical data for Mercury returned by MESSENGER (McCoy et al. 2018; Nittler et al. 2018) and planned from BepiColombo’s orbital mission (Rothery et al. 2020). Measurements of elements and minerals at the surface that are not detected from orbit will provide information about the entire mineral assemblage, allowing for a comprehensive interpretation of LRM deposits globally distributed across the planet.

Key Goal 4 Questions:

1. What does the surface of Mercury look like at the lander scale?
2. What processes shape the surface at scales of meters to tens of meters, and are those processes active today?
3. Are there landforms at the lander scale that we have yet to recognize from orbit, and if so, what do they tell us of the mechanisms that shape the Mercury surface today?
4. How do the surface expressions of the planet’s geology, composition, and interior properties at the lander scale fit into our global understanding of Mercury?

4. Science Objectives and Traceability

The purpose of this concept study was to evaluate the feasibility of a landed mission to Mercury in the near future that would accomplish groundbreaking science. As discussed in Section 3, there is no shortage of transformative science that can be done by the first landed mission to the innermost planet. Consequently, two overarching philosophies were adopted for this concept study:

1. *Evaluate a comprehensive, scientifically robust payload spanning the wide-ranging science measurements that could be made in situ on Mercury’s surface.* In particular, this study assured coverage of all four goals in generally equal detail, rather than choosing to focus on any one specific goal. The inclusion of a large number of instruments in the concept study provides a more valuable resource for the science community when planning a landed mission to Mercury in the future.

2. *Prioritize landing safely on Mercury.* Consistent with this philosophy, the team decided to focus resources on that fundamental challenge, without which landed science is not possible. As such, the team considered only payload implementations that leveraged previous development efforts, in particular those designed to perform in situ landed measurements on the Moon and Mars. The first landed measurements on the surface of Mercury are so fundamental that they can be made by current existing instrumentation, without the need for major development.

Table 1 provides traceability from the overarching four science goals to 14 specific science objectives, the measurements required to fulfill these objectives, and the functional requirements necessary to achieve these measurements. The functional requirements in Table 1 note constraints placed on the mission concept design by the payload.

5. Instrument Payload Description

An 11-instrument science payload (Figure 5) was chosen for this study, which satisfies the comprehensive science goals and objectives outlined in Table 1. This ambitious instrument suite is just one possible configuration that could accomplish the high-priority science goals we identify. Alternate payload implementations could be designed to return equally compelling science measurements. A future Mercury lander mission should not be limited to the science payload considered here, but rather should take advantage of technology advancements and use the best instrumentation available at the time of planning such a mission. The comprehensive payload listed in Table 1 is somewhat larger than those of previous New Frontiers missions. It may be advantageous to a proposed mission to reduce the payload or to consider foreign contributions. The only absolute requirement to achieve groundbreaking science from a Mercury lander is to perform in situ measurements on the surface of Mercury.

Analog instruments with their associated technology readiness level (TRL) numbers are also provided in Table 1. This section details the payload choices, describing the rationale and scientific measurements for the instruments selected for the concept study. Also described are two instruments included as a part of the engineering payload whose data could be used for opportunistic science. (Additional instruments were considered but, for a variety of reasons, were ultimately deemed unsuitable for this specific mission concept. See Ernst et al. 2020 for details.) The concept of surface operations, associated data

Table 1
Science Traceability Matrix

| Science Goals | Science Objectives | Measurement Requirements | Instrument (Analog [TRL]) | Functional Requirement |
|---|--|--|--|--|
| Goal 1: Investigate the highly chemically reduced, unexpectedly volatile-rich mineralogy and chemistry of Mercury's surface, to understand the earliest evolution of this end-member of rocky planet formation. | 1.1 Determine the major and minor elemental composition of the LRM, including its C content and volatile-element abundances (e.g., Na, K, S) | Absolute abundances of C, O, Na, Mg, Si, S, Cl, K, Ca, Fe, Th, U, Cr, Mn, if present at concentrations of >1 wt% | GRS: Gamma-Ray Spectrometer (MESSENGER [TRL 9], Psyche [TRL 7], MMX [TRL 7], Dragonfly [TRL 7]) | Continuous operation to avoid instrument degradation; unobstructed FOV of the surface; surface operations ≥ 72 hr |
| | 1.2 Determine the mineralogy of the components of the LRM, including any silicate, sulfide, or carbide phases that are present | Identification of silicates, sulfides, carbides, metallic phases, if present at concentrations of >1 wt% | XRD/XRF: X-Ray Diffractometer/X-Ray Fluorescence Spectrometer (MSL-CheMin [TRL 9], CheMin-V [TRL 6]) | Surface sample must be delivered into the XRD/XRF instrument |
| | 1.3 Investigate the chemical and mineralogical heterogeneity of the landing site | Measurements of Objective 1.2 from two locations at the landing site and from \geq two distinct surface disturbance events | | Ability to collect samples from multiple locations and to produce distinct surface disturbance events |
| Goal 2: Investigate Mercury's interior structure and magnetic field, to unravel the planet's differentiation and evolutionary history and to understand the magnetic field at the surface. | 2.1 Investigate the distribution of mass in Mercury's interior, determine the size and state of the core to characterize the solid and liquid portions, and search for seismic activity | Longitude libration amplitudes; obliquity | RS: Radio Science (InSight RISE [TRL 9]) | <i>Ka</i> -band communication to enable the most sensitive science measurements |
| | | Gravitational acceleration change due to solid-body tides; short-period seismic observations | MAC: Mercury Accelerometer/Short-Period Seismometer (InSight SEIS-SP [TRL 9]) | Positioned near surface; high data rate from continuous operations needed to detect potential seismic events |
| | 2.2 Measure the magnetic field at the surface to investigate the coupling between the dynamo and external field, the time variation of the field, the strength of the crustal field, and the electrical conductivity structure of the crust and mantle | Measurements of magnetic field at the surface as a function of time, with a precision of 1 nT and at cadence of 20 vector samples per second | MAG: Magnetometer (MESSENGER MAG [TRL 9]) | Positioned to minimize contributions from spacecraft-generated fields |
| | 2.3 Investigate the mineralogy of the surface to identify potential magnetic carrier minerals | | | Covered by Objective 1.2 mineralogical measurements above |

Table 1
(Continued)

| Science Goals | Science Objectives | Measurement Requirements | Instrument (Analog [TRL]) | Functional Requirement |
|--|--|---|---|--|
| Goal 3: Investigate the active processes that produce Mercury's exosphere and alter its regolith, to understand planetary processes on rocky airless bodies, including the Moon. | 3.1 Determine the composition and density of the near-surface neutral exosphere and compare with the surface compositional measurements, to investigate processes releasing materials from the surface | Densities of atomic and molecular species 1–100 amu, $M/\Delta M \sim 100$, sensitivity $\sim 1 \text{ count s}^{-1}$ at density of 10 cm^{-3} | NMS: Neutral Mass Spectrometer (BepiColombo STROFIO [TRL 9]) | Unobstructed FOV of space environment, angled 45° toward surface |
| | 3.2 Determine and characterize the incoming and outgoing fluxes of charged particles at Mercury's surface | Identification of low-energy charged particles, 1 eV e^{-1} to 20 keV e^{-1} , $M/\Delta M$ 4–40 over M/q 1–50, angular resolution $<20^\circ$ | IMS: Ion Mass Spectrometer (MESSENGER FIPS [TRL 9]) | Unobstructed FOV of space environment, angled 45° away from surface |
| | | Identification of high-energy charged particles, 20 keV – 1 MeV , angular resolution $<20^\circ$ | EPS: Energetic Particle Spectrometer (New Horizons PEPSSI [TRL 9]) | Unobstructed FOV of space environment, angled 45° away from surface |
| | 3.3 Determine and characterize the influx of micrometeoroids (dust) at Mercury's surface | Measurements of dust flux with sensitivity to measure $10^{-15} \text{ kg m}^{-2} \text{ s}^{-1}$ | DD: Dust Detector (New Horizons SDC [TRL 9]) | Unobstructed FOV of space environment, looking toward zenith |
| | 3.4 Investigate the nature of Mercury's regolith, including particle sizes and heterogeneity | Images of regolith in ≥ 3 visible colors, pixel scales $\leq 500 \mu\text{m}$ @ 1 m distance | FootCam: Regolith Imagers (Malin Space Science Systems, ECAM [TRL 9]) | Mounted to resolve 1 mm grains; LED illumination @ 450, 550, 650, 750 nm |
| 3.5 Investigate the characteristics of space weathering on Mercury | Measurements for Objective 1.2 and 3.4 repeated for \geq two distinct surface disturbances of the same location | | Ability to collect multiple samples from the same location and to produce distinct surface disturbance events | |
| Goal 4: Characterize the landing site, to understand the processes that have shaped its evolution, to place the in situ measurements in context, and to enable ground truth for global interpretations of Mercury. | 4.1 Connect observations from images acquired by orbiting spacecraft to those from the lander and determine the geological context of the landing site | Images of landing site acquired during descent, pixel scales 1 cm to 1 m | DescentCam: Descent Imagers (Malin Space Science Systems, ECAM [TRL 9]) | Periodic imaging of the surface during descent; two cameras oriented 90° from one another to enable surface imaging despite changing orientation during descent |
| | 4.2 Characterize the geological setting of the landing site, including heterogeneity and landforms, and search for changes over the mission by surface, horizon, and exosphere imaging | Images of the landing site, pixel scale $\leq 5 \text{ cm}$ within 50 m; $\geq 180^\circ$ az, 0° to -45° elev | StaffCam: Panoramic Imager (MER Pancam [TRL 9], MSL Mastcam [TRL 9]) | Unobstructed access to $\geq 180^\circ$ of the landing site; articulation to achieve angular coverage |
| | 4.3 Characterize the bulk-element composition of the local landing site and place it into context with the equivalent orbital measurements | | | Covered by Objective 1.1 elemental measurements above |

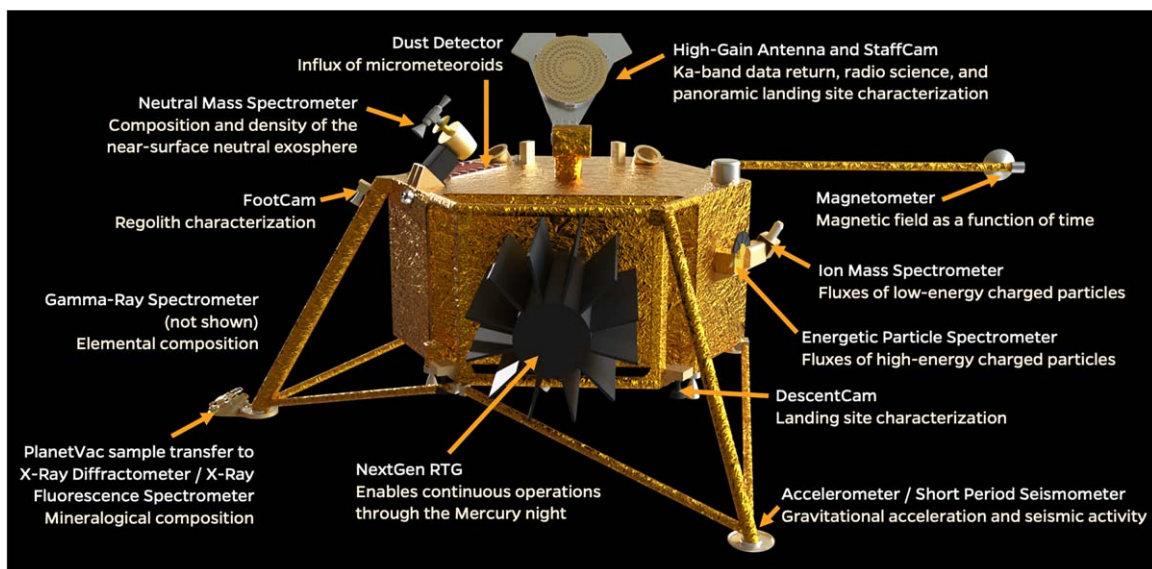


Figure 5. The Mercury Lander spacecraft concept in its landed configuration. The placement of the 11-instrument payload, RTG, and high-gain antenna are shown.

volume and margin for the landed phase of the mission, and implications for contingency in science data rates and instrument operation options are discussed in Section 7.3.

5.1. Geochemistry Payload

The instrument payload we selected for this mission concept study to address Goal 1 (Geochemistry) includes a GRS and an X-ray diffractometer/X-ray fluorescence spectrometer (XRD/XRF). XRD/XRF analysis requires delivery of surface samples into the instrument; this is accomplished via the PlanetVac sampling system.

5.1.1. Gamma-Ray Spectrometer

Data from the GRS will be used to determine bulk elemental abundances of the materials at the landing site, to a depth of tens of centimeters. High-resolution, in situ data will yield tighter constraints than data obtained from orbital missions for understanding Mercury's geochemistry and provide insights into the volatile-rich nature of the planet and its thermal and magmatic evolutionary history. The GRS data will also offer a crucial ground truth for the orbital elemental measurements made by the MESSENGER and BepiColombo GRS and XRS instruments. The GRS is a high-purity, germanium-based sensor that makes high-energy-resolution measurements of gamma-ray emissions from Mercury's surface. The instrument selected for this concept study is based on the MESSENGER GRS (Goldsten et al. 2007), with updates from ongoing GRS instrument development for the upcoming Psyche (Lawrence et al. 2019a) and Martian Moons eXplorer (MMX; Lawrence et al. 2019b) missions. For this study, the GRS design is simplified, removing the anticoincidence shield and incorporating a low-power Ricor cryocooler. This simplified design is made possible by the higher signal-to-noise ratio that is achieved via landed measurements compared with orbital measurements.

The GRS will measure gamma-ray emissions from Mercury's surface that result from cosmic-ray bombardment of near-surface materials. The cosmic rays liberate neutrons, which interact with atomic nuclei to produce element-specific

gamma-ray emissions. The GRS will measure gamma-ray emissions from major and minor elements (O, Mg, Si, Al, Ca, Fe, C, Na, S, Ti, and Mn) and naturally radioactive elements (K, Th, and U). These gamma-ray emissions will be used to characterize the elemental composition of Mercury's surface, in a $\sim 1 \text{ m}^3$ volume beneath the lander, following procedures developed for the analysis of GRS data from the Near Earth Asteroid Rendezvous (NEAR; Peplowski et al. 2015; Peplowski 2016) and MESSENGER (Peplowski et al. 2011, 2012, 2014, 2015) missions. Landed, in situ measurements will improve statistical uncertainties of many elements measured in MESSENGER data. For example, measurements of the concentrations of Na, Mg, Si, S, Cl, Fe, Cr, and Mn, if present at concentrations of $>0.5 \text{ wt}\%$, will be completed with better than 10% statistical uncertainties. If present at concentrations of $>1 \text{ wt}\%$, measurements of the concentrations of C, O, and Ca will be completed with better than 20% statistical uncertainties. Measurements of the concentration of K, if present at $>100 \text{ ppm}$ concentration, will be collected with better than 10% statistical uncertainty. The concentrations of Th and U, if present at $>10 \text{ ppb}$ concentrations, will be measured with better than 20% statistical uncertainty. By improving on the statistical uncertainties and characterizing the composition of the local region, the GRS will provide valuable context for the measurements made by the XRD/XRF instrument, which samples smaller regions.

Measurements of the concentration of Al will be complicated by the substantial presence of this element in the instrument housing and local lander structural materials. The MESSENGER GRS was able to measure aluminum at 7 wt% with an uncertainty of $\sim 30\%$. This measurement was made possible by considerable data reduction and analysis (Peplowski et al. 2012). A landed measurement will benefit from lower backgrounds and higher signal from the planet compared with an orbital measurement. Al concentration will be detectable by the landed GRS, and it is likely that the Mercury Lander will measure Al concentration more precisely than MESSENGER. The detection limits are difficult to define without detailed knowledge of the spacecraft material local to the GRS, and so,

under this implementation, measurements of Al by the GRS on the Mercury Lander will be done on a best-effort basis.

5.1.2. X-Ray Diffractometer/X-Ray Fluorescence (XRD/XRF) and PlanetVac

A combination XRD/XRF spectrometer provides both mineralogical and elemental characterization of the regolith at the landing site (Blake et al. 2019). Powder XRD is a powerful crystallographic technique that, in combination with Rietveld refinements and full-pattern fitting methods, can be used to quantify crystalline and X-ray amorphous components, crystallite size and strain, and unit-cell parameters (e.g., Bish & Howard 1988; Chipera & Bish 2002). The refined unit-cell parameters of minerals can be used to infer crystal chemistry because ionic substitution within a lattice affects the unit-cell lengths and angles (e.g., Morrison et al. 2018). XRF spectroscopy is a geochemical technique used to quantify major, minor, and trace elemental abundances within a sample.

The combination of XRD and XRF measurements will directly address the goal to investigate the highly chemically reduced, unexpectedly volatile-rich mineralogy and chemistry of Mercury's surface. XRD data will be used to identify and quantify the Mg-rich silicates, oxides, sulfides, and metals predicted to be on the surface of Mercury (Stockstill-Cahill et al. 2012; Vander Kaaden & McCubbin 2016; Namur & Charlier 2017), as well as other minerals on the surface, to a detection limit of ~ 1 wt%. The refined unit-cell parameters of minerals will be used to identify crystal chemistry (e.g., Morrison et al. 2018), which is important for understanding magmatic evolution on Mercury. Minor and trace elements derived from XRF measurements will inform elemental substitutions within minerals. Even if there is an unknown mineral on Mercury's surface, XRD patterns could be used to solve the crystal structure.

Space weathering and impact processes may create abundant amorphous materials in the regolith (e.g., Domingue et al. 2014). Diffraction data can be used to quantify the abundance of amorphous materials at the surface (e.g., Rampe et al. 2020). Furthermore, the composition of the amorphous materials can be estimated from mass balance calculations using mineral abundances and crystal chemistry from XRD data and bulk elemental abundances from XRF data (e.g., Rampe et al. 2020). Combining information about the amount of amorphous material at the surface and its composition will help to place tighter constraints on the space weathering environment at Mercury.

The CheMin-V instrument, designed for the Venera-D Venus mission concept and drawing heritage from the CheMin instrument on the Mars Science Laboratory (MSL) Curiosity rover (Blake et al. 2012, 2019), was adopted for this study. MSL-CheMin is a combination XRD/XRF that operates in transmission (i.e., Debye-Scherrer) geometry. MSL-CheMin accepts a few tens of milligrams of drilled rock powders and soils, sieved to $<150 \mu\text{m}$, or drilled rock powders delivered directly from the drill bit to the instrument (Blake et al. 2012; Rampe et al. 2020). CheMin-V will improve on CheMin by acquiring data more rapidly with improved angular resolution and by collecting quantitative XRF data (Blake et al. 2019), thereby improving the identification of minerals. The instrument will have two reusable sample cells that can be analyzed simultaneously. Diffraction data will be collected on charge-coupled devices (CCDs), and XRF data will be collected on

silicon drift detectors. Full XRD/XRF analyses will be completed within 1 hr.

XRD/XRF analysis requires that the sample be transferred to the instrument; for Mercury Lander this is accomplished via the PlanetVac sampling system (Zacny et al. 2014). PlanetVac is the sampling instrument of choice for other planetary sampling firsts, such as sample return from Phobos by the MMX mission (Zacny et al. 2020), analysis of the lunar surface via NASA's Commercial Lunar Payload Services (CLPS) program, and pneumatic sample transfer on the surface of Titan on NASA's Dragonfly mission (Turtle et al. 2019).

Regolith is collected by the PlanetVac pneumatic samplers, which are mounted on two of the lander feet (Figure 5). This configuration will allow sampling from two distinct surface locations for characterizing differences and similarities between the two sample sites, as well as for redundancy and robustness. The pneumatic samplers use pressurized gas to loft regolith and pass it through tubes to the XRD/XRF analysis chamber. Nozzles directing the compressed gas flow from the sampler cone loosen and loft surface material into the pneumatic sample transfer lines. Here, the sample is transferred by the pressure differential caused by the released compressed gas and the environmental vacuum at the transfer lines' exhaust.

Providing this pressure differential is an onboard compressed gas canister sized to accommodate eight sample collection operations, four per sampling system, with margin. At the sample ingest position, a deflector plate is used to siphon the transferred sample into the XRD/XRF analysis cell. The cell is self-metering and will accept ~ 100 mg of regolith. MSL-CheMin has demonstrated that bulk powder diffraction measurements of samples with particle sizes $<150 \mu\text{m}$ produce the best diffraction patterns (Blake et al. 2012). Larger size fractions can result in poor grain motion and/or bright spots on the Debye rings that negatively influence mineralogical interpretations from the patterns. A $150 \mu\text{m}$ screen is placed above the cell such that only the $<150 \mu\text{m}$ size fraction enters the cell. Once filled, any additional transferred particles will flow naturally around the deflector plate and out to an exhaust. This approach is well suited for instruments that require an extremely small and known sample volume (Zacny et al. 2012). XRD/XRF instrument analysis can be used to confirm successful sample transfer and thus can further simplify the sampling system, by removing the need for onboard sensors to image sample transfer.

The architecture of the PlanetVac sampling system allows for more than one part of the landing site to be sampled. By carrying two independently operated sample acquisition systems on separate lander legs, a lateral sampling distribution will be obtained from two distinct surfaces. A vertical sampling profile will also be obtained by allowing the sampler to "burrow" into the regolith, achieved with a longer-duration compressed gas release at the nozzle. Cross-contamination is mitigated by flushing the pneumatic lines between sampling events with gas, to clear residual material. The reusability of the XRD/XRF cells allows for multiple samples from each PlanetVac cone to be analyzed. Measurements from distinct PlanetVac cones will be used to determine the mineralogy and geochemistry of the regolith from two different locations at the landing site. Multiple samples from a single PlanetVac will be used to investigate compositional changes with depth (see also Section 5.3.4). Each sampling event also doubles as a surface

disturbance event. The full operations planned for the geochemical instruments are discussed in Section 7.3.

5.2. Geophysics Payload

The instrument payload we selected for this mission concept study to address Goal 2 (Geophysics) includes a radio science (RS) investigation (part of the telecommunications subsystem, and so not counted as one of the 11 science instruments), a magnetometer (MAG), and an accelerometer (which we abbreviate as MAC for the Mercury Accelerometer).

5.2.1. Radio Science

RS utilizes the onboard telecommunications system to establish a coherent two-way link between stations on Earth and the lander. This link allows the measurement of distances between the stations and lander (ranging data) or, by using the Doppler effect, the measurement of the line-of-sight velocity between stations and lander (Doppler data). RS investigations are a common part of planetary missions, as the enabling equipment (i.e., a radio) is needed for deep-space navigation. In addition, RS data have been used to infer the gravitational fields of objects throughout the solar system, providing critical constraints on the interior structure of these objects. Although most of these investigations have involved an orbiting spacecraft, the Viking, Pathfinder, and InSight missions to Mars have provided a consistent set of data with which to refine Mars's orientation and infer its interior structure (Folkner et al. 1997, 2018; Yoder & Standish 1997; Yoder et al. 2003; Konopliv et al. 2006, 2011; Kuchynka et al. 2014; Jacobson et al. 2018).

This lander concept study has the capability for both *X*-band (8–12 GHz) and *Ka*-band (26–42 GHz) measurements, with the latter providing data with less noise and less susceptible to interference from solar plasma (e.g., Bertotti et al. 1993; Asmar et al. 2005, 2019; Iess et al. 2012). The use of *Ka*-band data with proper calibration for effects from, for example, Earth's atmosphere and solar plasma will allow the determination of the line-of-sight velocity with a precision close to 0.01 mm s^{-1} at a 60 s integration time (e.g., Iess et al. 2012, 2018; Asmar et al. 2019). For comparison, InSight currently uses an *X*-band system (Folkner et al. 2018), which in general has a precision close to 0.1 mm s^{-1} at a 60 s integration time. Data will be collected on a daily basis during contact periods, with data sessions planned for continuous 24 hr communications. As described in Section 7.3, there are two distinct communication periods in the mission lifetime, which will allow for the collection of measurements at different times with the planet in a different orbital phase.

From these Doppler measurements to a fixed location on Mercury, changes in the planet's orientation can be measured precisely. Using Viking ranging data, Yoder & Standish (1997) were able to determine Mars's precession rate, which, combined with the planet's gravitational flattening (J_2) coefficient, results in a measurement of the planet's moment of inertia and thus a measure of radial density distribution within the planet. Using additional Pathfinder measurements, Folkner et al. (1997) were able to improve the error on the moment of inertia by a factor of 10. For Mercury, the moment of inertia has been determined by virtue of the planet being in an equilibrium state called the Cassini State I (e.g., Peale 1976; Margot et al. 2012, 2018; Genova et al. 2019). An improved measurement of the moment of inertia can be obtained by

determining the planet's longitudinal librations. To date, these librations have been measured from Earth-based radar observations (Margot et al. 2007) and gravitational harmonics from the tracking of MESSENGER's orbit (Smith et al. 2012; Genova et al. 2019). Precise measurements from a fixed position on the planet can be used to improve knowledge of the longitude librations, and thus further improve our knowledge of the moment of inertia of Mercury. Such measurements would, in turn, provide additional constraints on Mercury's interior structure and current thermal state.

5.2.2. Magnetometer (MAG)

Surface measurements of the vector magnetic field can be used to address questions regarding Mercury's magnetic field, help elucidate interior structure, and improve our understanding of exospheric processes such as surface precipitation. Continuous vector magnetic field observations over the duration of landed surface operations will enable identification of both static and time-varying fields. Magnetospheric processes occur over a wide range of timescales, from subseconds to a Mercury solar day, and the magnetometer will thus measure the magnetic field at 20 samples per second (sps), returning this full data stream to Earth. Onboard down-sampling to 1 sps, for example, together with calculation of a 1 sps data stream that captures the root-mean-square fluctuation at frequencies above 1 Hz, can yield a lower data volume for times of more limited downlink capability if needed. Suitable heritage instruments include the MESSENGER magnetometer (Anderson et al. 2007) and the InSight magnetometer (Bandfield et al. 2019), which is being adapted for use on the Europa Clipper mission. The MAG is mounted at the end of a boom that is deployed after landing (Figure 5), to minimize contributions from spacecraft-generated fields. A star camera, colocated at the end of the boom, will provide magnetometer orientation information, and a dedicated small sunshield and heater are needed to maintain the magnetometer temperature within the instrument operating range (approximately -50°C to $+50^\circ\text{C}$). In addition, prelaunch spacecraft magnetic cleanliness and magnetic characterization protocols (e.g., Bandfield et al. 2019) should be employed.

During the period of surface operations, local time, heliocentric distance, and solar wind conditions will all affect the magnetic field recorded at the landing site. Superposed on this background time-varying field will be the effects of crustal magnetization. Crustal field models based on MESSENGER data suggest that contributions to the surface field strength from crustal magnetization may be on the order of tens of nanoteslas (nT). However, these models cannot capture the shortest wavelengths in the field, and experience from the InSight mission indicates that the surface crustal field can be considerably stronger than satellite predictions, providing important constraints on estimates for local magnetization (Johnson et al. 2020). The MAG will measure Mercury's magnetic field with a precision of 1 nT. Although MESSENGER offered no constraints on the southern hemisphere crustal field, BepiColombo may do so toward the end of the MPO lifetime (if periapsis at that time is in the southern hemisphere). Such measurements would provide helpful regional context for crustal fields in the vicinity of our selected landing site.

5.2.3. Accelerometer (MAC)

Accelerometers, depending on design characteristics, are used to measure vibrations, motions, and changes in gravity and hence can function as seismometers and/or gravimeters. Potential analog instruments considered for this payload include the Rover Inertial Measurement Units (IMUs) from MSL, which are Northrup Grumman LN-200S units (e.g., Lewis et al. 2019) and the InSight SEIS-SP short-period seismometer (Pike et al. 2018; Lognonné et al. 2019). The latter instrument has the demonstrated ability to measure quake signals (Lognonné et al. 2020) and solid-earth tides (Pike et al. 2018) and represents an appropriate analog capable of multi-purpose operation for both short-period seismic observations and measurement of the gravitational acceleration change from solid-body tides.

The Mercury Accelerometer (MAC) provides direct measurements of the gravitational changes due to tides over the course of the landed mission. The instrument will measure accelerations in three axes with low noise (SEIS-SP can operate at $0.25 \text{ ng Hz}^{-1/2}$) and collect continuous data at up to 100 sps. Measurements of acceleration changes in the vertical direction will also resolve the changes in the vertical acceleration of gravity at the landing site surface due to tidal variations. These point measurements, when combined with RS tracking data for this mission and the global orbital data from MESSENGER and BepiColombo, will robustly resolve the k_2 tidal Love number, which is a reflection of the rheological behavior of the interior (e.g., Padovan et al. 2014; Steinbrügge et al. 2018). Further, when combined with data for the moment of inertia from RS and the value of h_2 tidal Love number that describes actual surface displacements because of tides, a precise k_2 value can be used to tightly bound estimates of the size of an inner core (Steinbrügge et al. 2018).

High-frequency measurements from the accelerometer allow it to operate as a short-period seismometer, enabling the first observations of the seismicity of Mercury. As a one-plate planet, Mercury's seismicity may be comparable with that of Mars, which is similar to the seismicity of intraplate regions on Earth (Giardini et al. 2020). Mercury is rife with tectonic features related to the planet's global contraction (Byrne et al. 2014; Watters et al. 2016), including geologically young scarps $< 50 \text{ Myr}$ indicative of ongoing shortening deformation. Further, similar to the Moon, tidally induced quakes are also likely. Indeed, the largest expected tidal displacements on Mercury at $\sim 2.4 \text{ m}$ (Steinbrügge et al. 2018) are at least an order of magnitude larger than they are on the Moon at $\sim 0.1 \text{ m}$ (Williams & Boggs 2015). Should Mercury have a seismic behavior similar to Mars (where InSight found 174 quakes in its first 10 months: Giardini et al. 2020), it would be reasonable to expect the detection of several tens of quakes on Mercury over a roughly 88-day landed mission. Those quakes would contain information about the nature of the crust and tectonics on Mercury and have the potential to place bounds on estimates of the depth of the core from the strength of the ScS core–mantle boundary reflected waves from the shallow core (Stähler et al. 2017). Such data are necessary to help us to better understand the planet's structure and evolution, including whether or not Mercury continues to contract today.

5.3. Space Environment Payload

The instrument payload we selected in this mission concept study to address science Goal 3 (Space Environment) includes a neutral mass spectrometer (NMS), an ion mass spectrometer (IMS), an energetic particle spectrometer (EPS), a dust detector (DD), and regolith imagers (FootCam).

5.3.1. Neutral Mass Spectrometer (NMS)

The NMS measures the densities of neutral species in the exosphere, including those of both atoms and molecules. Atomic species are important to quantify because they represent those that have been observed remotely from Earth-based telescopes and/or by MESSENGER. Molecules are an important aspect of the neutral measurements because both Earth-based and MESSENGER measurements suggest that some higher-energy exospheric atoms, particularly Ca, achieve those energies via the photodissociation of a molecule released during micrometeoroid impact vaporization (MIV; e.g., Killen et al. 2005; Burger et al. 2014). Because molecules generally emit radiation less efficiently than atoms, their detection around Mercury is difficult, and no neutral molecule has yet been detected.

Given the key but unexplored role that molecules play in sourcing the exosphere, an NMS instrument is needed to make these measurements. Although it would be desirable to have a mass range out to ~ 150 atomic mass units (amu) to cover Xe (as the noble gases are important tracers of planetary evolution), resource limitations of a lander preclude such an instrument. An NMS with a range of ~ 100 amu is sufficient to cover the majority of atoms (i.e., $\leq \text{Ni}$) and molecules (e.g., MgS, CaS) that would likely be detected. Similarly, whereas a high mass resolution would enable some potential ambiguities to be resolved if the molecules happened to overlap in mass space, a mass resolution ($M/\Delta M$) of ~ 100 is reasonable for a small NMS. Finally, the sensitivity of the NMS needs to be high, of order one count per second at density of 10 cm^{-3} (Orsini et al. 2021). The analog used for this mission concept study is Strofio on the BepiColombo mission (Orsini et al. 2021). The NMS is mounted on the lander with an unobstructed field of view (FOV) to the space environment and angled toward the surface (Figure 5).

5.3.2. Ion Mass Spectrometer (IMS) and Energetic Particle Spectrometer (EPS)

Measurements to characterize the low-energy ions at Mercury's surface are made with an IMS. An EPS measures ions with energies up to 1 MeV per nucleon, as well as energetic electrons. Together, these instruments will measure ions incidental to the surface, from the magnetosphere, and released from the surface by MIV and/or sputtering.

Mercury's magnetosphere is surface bounded because the collisionless exosphere (which is also surface bounded) does nothing to impede the flow of plasma. At midlatitudes on the nightside, magnetospheric plasma, mostly protons and electrons, is expected to impact the surface after being accelerated planetward by magnetic reconnection in the magnetotail. The location and intensity of this magnetotail plasma precipitation depend on the state of the magnetosphere, which can vary on timescales of seconds to hours owing to changing inputs from the solar wind. The flow of protons toward the surface has been characterized, with energies up to the 13 keV maximum that

could be measured by MESSENGER (Dewey et al. 2018). Planetary ions present in the magnetotail (e.g., Na^+ , O^+ , and He^+) are also likely accelerated toward the surface, potentially at much higher energies owing to their increased mass. For example, Na^+ ions would be up to 23 times higher in energy than the corresponding protons in the flow. Modeling of the Mercury magnetosphere shows that these energies may go as high as 100 keV (Delcourt et al. 2003). Although a minor component of the magnetotail, <10% by number (Gershman et al. 2014), these high-energy species are important to measure because they are much more efficient at ion sputtering on the surface. MESSENGER measurements of X-ray fluorescence from the surface are likely direct evidence of electron impacts, probably in the 1–5 keV range (Starr et al. 2012; Lindsay et al. 2016). Electrons were measured in Mercury’s magnetotail at energies ranging from 10 to 300 keV (Ho et al. 2012, 2016; Lawrence et al. 2015; Baker et al. 2016; Dewey et al. 2017) and at energies <10 keV (Slavin et al. 2008; Ho et al. 2011; Starr et al. 2012). The complex, time-varying dynamics of Mercury’s magnetosphere make extrapolating plasma measurements, taken from orbit, down to the surface complicated except in certain regions (e.g., at magnetospheric cusps). Flux measurements of incoming ions and outgoing neutrals at the surface, even from a single location, would greatly improve knowledge of these processes and add critical constraints to models of exogenic processes and space weathering.

Typical planetary IMS instruments measure ions in the 1 eV e^{-1} to 60 keV e^{-1} range, but these instruments often have a limited FOV when not on a spinning spacecraft. Ideally, the IMS would have a large simultaneous FOV to allow for concurrent measurements of ions incident to, as well as upwelling from, the surface along with sufficient angular resolution to distinguish the two sources (<20° angular resolution). The vast majority of the ions will likely be <20 keV e^{-1} , so an instrument with a large simultaneous FOV but a limited energy range would be more suitable. The IMS should have sufficient mass resolution to distinguish among the known and expected planetary ions (e.g., Mg^+ and Na^+ ; K^+ and Ca^+) and an $M/\Delta M$ of >4 for singly charged ions. The EPS can cover the higher energy range for ions, up to 1 MeV per nucleon, as well as energetic electrons. Measuring only particles incident on the surface, the EPS does not need such a broad FOV as the IMS; however, angular resolution of <20° would be helpful in understanding processes at the surface. Ions released directly from the surface through MIV and/or sputtering are also important to measure, as they allow for a complete accounting of the species driven from the surface by all the processes combined. These ions are likely in the 1–10 eV energy range and could be measured by either the IMS or, potentially, the NMS if it has a low-energy-ion mode. Analogs for the IMS and EPS instruments are the Fast Imaging Plasma Spectrometer (FIPS) on board MESSENGER (Andrews et al. 2007) and the Pluto Energetic Particle Spectrometer Science Investigation (PEPSSI) on board New Horizons (McNutt et al. 2008), respectively. The IMS and EPS are both mounted with an unobstructed view to the space environment and angled away from the surface (Figure 5).

5.3.3. Dust Detector (DD)

The third objective of Goal 3 is to characterize the incoming dust flux at the surface. Knowing the population of incoming dust is critical for completing the inventory of exospheric

source processes, for understanding the space weathering environment at Mercury, and for the development of models of regolith production and gardening. MIV has been shown to be the primary process most likely behind the production of both Ca (Burger et al. 2012, 2014) and Mg (Merkel et al. 2017) in Mercury’s exosphere. Furthermore, the Ca source rate has shown a strong correlation with the passage of Mercury through the dust trail of comet 2P/Encke (Killen & Hahn 2015). Measurement of the dust flux at the surface is therefore a crucial, missing piece in our knowledge of the MIV source of exospheric material.

Models of the dust environment around Mercury provide some insight into the dust flux to the surface. Based on Pokorný et al. (2018), we would expect the average flux of meteoroids on Mercury to be 12.16 ± 3.54 metric tons ($12,160 \pm 3540$ kg) per day. The average vaporization flux is thus $(200 \pm 16) \times 10^{-15} \text{ kg m}^{-2} \text{ s}^{-1}$, with the flux mostly in smaller meteoroids with diameter less than 400 μm . BepiColombo does have a dust instrument (Nogami et al. 2010; Kobayashi et al. 2020) and will provide valuable observations. However, the importance and advantage of measurements taken by a landed instrument is that the incoming dust flux will be obtained simultaneously in both space and time with the other exospheric measurements, allowing for the establishment of correlations between dust and species release and thus a better understanding of the direct effects of MIV on the surface—critical observations for understanding the nature of space weathering at Mercury in general.

Although measurements of particle sizes and impact energies would be valuable, the primary goal is to measure the flux, with sensitivity to measure $10^{-15} \text{ kg m}^{-2} \text{ s}^{-1}$ (roughly two orders of magnitude smaller than the current modeled average fluxes, to provide sufficient sensitivity to expected variations in the flux over Mercury’s surface as a function of local time). The dust detector is envisioned as a simple sampling array, akin to the Student Dust Counter (SDC) on New Horizons (Horányi et al. 2008), to count the flux of picogram- to nanogram-size dust particles incident on the surface. To have a clear view to space, the dust detector is placed on the top deck of the lander (Figure 5).

5.3.4. Regolith Imager (FootCam)

Mercury Lander’s regolith imagers (FootCam) will be used to characterize the regolith and to search for local changes to the regolith induced by the PlanetVac system (which can mobilize regolith surrounding each sampler cone). FootCam consists of two monochrome cameras mounted on two of the three spacecraft landing legs and positioned to observe the corresponding lander foot and surrounding area (Figure 5). Four-color LED arrays provide illumination to each FootCam imager, with colors attuned to geologically appropriate wavelengths (notionally 450, 550, 650, and 750 nm). The number and placement of the LEDs will be designed to optimize nighttime imaging of both FootCam (required) and StaffCam (as possible) (see Section 5.4.2). The FootCams are positioned such that each can observe both the contact of the lander foot with the surface and the associated PlanetVac sampling system. Malin Space Science System (MSSS) ECAM, 5 megapixel CMOS cameras ($44^\circ \times 35^\circ$ FOV and 0.3 mrad iFOV), with heritage from the Mars Exploration Rover (MER) and MSL missions, were selected for this payload.

FootCam will return images of the landing pads to provide insight into the regolith properties encountered by the lander, including grain size, heterogeneity, and any changes due to surface disturbance events. These images, with a pixel scale of approximately $360\ \mu\text{m}$, will help to inform geological studies of the landing site, including characterization of the cohesion, mechanical strength, and texture of the “soil.” Repeated imaging during the entire duration of operations will also allow for changes in the local surface materials to be detected. FootCam images will give information on the texture and size distribution of particles in the regolith, which will provide important insights into the maturation of the regolith on submillimeter to centimeter scales.

Previous tests indicate that each PlanetVac sampling event will likely mobilize sufficient amounts of regolith to produce observable changes to the surface surrounding each sampler cone (Zacny et al. 2010, 2014). FootCam will image the immediate area surrounding each corresponding lander foot before and after each sampling event, to search for any surface disturbance induced by the PlanetVac system or by ongoing surface processes.

The extent of material disturbance during each sample event can be used to infer the mechanical properties of the regolith (e.g., cohesion). Color imaging will help reveal whether fresher, unweathered (i.e., brighter) material is disturbed from immediately below the surface and exposed during sampling. Thus, in addition to providing information on the success of each sampling event, FootCam images will return valuable information on the nature of Mercury’s regolith and the depth and degree of space weathering on the surface.

5.4. Geology Payload

The instrument payload we selected in this mission concept study to address Goal 4 (Geology) includes cameras to resolve the surface during the lander’s descent (DescentCam) and a panoramic camera mounted atop the lander to survey the landscape (StaffCam).

5.4.1. Descent Imagers (DescentCam)

Two monochrome descent imagers (DescentCam) will characterize the landing site, linking it to existing, global maps of the planet via a set of nested images acquired during the descent and landing sequence. The two cameras are oriented with their FOVs 90° from one another, ensuring that the surface remains in view and can be imaged even as the lander changes orientation relative to the surface during descent. For this mission concept study, the MSSS ECAM 5 megapixel (2650×1944) CMOS cameras ($44^\circ \times 35^\circ$ FOV and $0.3\ \text{mrad}$ iFOV) were adopted, drawing on heritage from the MER and MSL missions (as for FootCam for Goal 3). The descent cameras will return a set of nested images of the landing site locale and region at different scales—with estimated pixel scales of $6\ \text{m}$ at $20\ \text{km}$ altitude, $30\ \text{cm}$ at $1\ \text{km}$ altitude, and $0.6\ \text{mm}$ at $2\ \text{m}$ altitude—playing a critical role in bridging the gap between orbital-scale MESSENGER and BepiColombo data and lander-scale observations from the ground. These descent images will also assist in determining precisely the landing site itself.

5.4.2. Panoramic Imager (StaffCam)

The panoramic imager (StaffCam) will characterize the geological setting of the landing site. StaffCam is a monochrome camera colocated with the gimbaled high-gain antenna (Figure 5). This mounting location, which extends up from the main body of the lander, enables panoramic imaging of the landing site (although Sun “keep-out” zones will prevent a full 360° panorama from being acquired before dusk). For this concept study, StaffCam was selected to be the same as cameras with heritage from the MER Pancam and MSL Mastcam, both of which comprise a MSSS ECAM, 5 megapixel CMOS camera or equivalent. The concept of operations for StaffCam assumes a $\sim 2650 \times 1944$ pixel sensor imaging with a $44^\circ \times 35^\circ$ FOV and $0.3\ \text{mrad}$ iFOV. Some of the LEDs required for FootCam will be mounted in such a way to enable illumination of the surface around the lander through the Mercury night, as possible. StaffCam will survey the landing site from the near field to the horizon, imaging the morphology of the site and the surrounding landscape at pixel scales of $1.5\ \text{cm}$ from a distance of $50\ \text{m}$. StaffCam will acquire a set of complete 360° panoramas (when able) via a series of nine overlapping images; areas of overlap will permit the generation of stereo scenes.

The panoramas, coupled with data from the descent imager, place the landing site-scale morphology and geology within the context offered by orbital imaging from previous and future missions. Photometric analysis of areas viewed under differing illumination will offer clues to the soil texture, porosity, etc., as well as the scattering properties of regolith particles. StaffCam images of the horizon under post-dusk and pre-dawn illumination conditions may help identify and characterize dust particles from electrostatic levitation or thermal lofting. Mid-Mercury-night imaging of the sky will be used to attempt to detect the faint sodium emission of the Mercury nightside exosphere (i.e., the “tail” region) near its maximum likely extent and intensity. This exosphere imaging campaign is considered opportunistic; whether or not an adequate signal-to-noise ratio can be attained using this light source will be validated by radiometric modeling before flight. Repeated StaffCam images of the near and far field will also allow detection of possible changes in the vicinity of the landing site, perhaps due to activity of the lander (e.g., resulting from PlanetVac operations) or other events/processes such as mass wasting or localized tectonic activity from, for instance, thermal loading.

5.5. Engineering Payload

Two instruments included on the spacecraft are classified as engineering instruments to aid with site selection and landing: a narrow-angle camera (NAC) on the orbital stage, and a light detection and ranging (LIDAR) instrument on the lander. Data acquired by these instruments will be downlinked in full and can be used to support the mission’s science.

5.5.1. Orbital Narrow-angle Camera

A narrow-angle camera is included on the orbital stage to enable landing site reconnaissance in the orbital phase. For this mission concept study, the NAC is based on the Lunar Reconnaissance Orbiter Camera (LROC) NAC (2.85° FOV and $0.01\ \text{mrad}$ iFOV; Robinson et al. 2010). Opportunistic imaging enables landing site reconnaissance, supplementing BepiColombo’s $3\ \text{m}\ \text{pixel}^{-1}$ imaging capability with $1\ \text{m}\ \text{pixel}^{-1}$ scale

of the landing area from 100 km altitude. These images are used for down-selection of a safe landing zone.

5.5.2. LIDAR

To successfully land on the surface of Mercury, onboard hazard avoidance will be implemented, as the site itself will not be characterized at the scale of the lander prior to descent. The Mercury Lander will carry a LIDAR instrument as a required engineering component of the landing design, and thus engineering considerations drive the choice of the specific LIDAR selected. For this concept study, the LIDAR selected is one manufactured by Kodiak with flight heritage. However, the LIDAR would also provide opportunistic science. In addition to characterizing the topography of the local landing site, the LIDAR data can provide information regarding shape, surface roughness, and reflectivity of the Mercury surface at a variety of scales, augmenting the science return of the descent camera and other imaging instruments.

6. Landing Site

A driving scientific goal of this study is to perform in situ measurements of Mercury’s surface, with a particular interest in measuring the LRM, as this material may incorporate the planet’s ancient, graphite-rich flotation crust. Prospective landing sites are therefore necessarily restricted to areas of the planet where LRM is exposed (Figure 1). In this section, we discuss the current best characterization of this landing site based on MESSENGER data and then briefly review the data BepiColombo is positioned to acquire that will further our understanding of the location.

The principal requirement for the landing site for this mission study was that it be in a region with extensive LRM deposits. We further refined the site selection based on thermal considerations and direct-to-Earth communication opportunities during the time frame of the landed operations (as detailed in the main technical report; Ernst et al. 2020). The site ultimately selected for this study is located at approximately 40°S, 178°E.

6.1. MESSENGER Landing Site Characterization

The landing site region contains substantial exposures of LRM (Figure 1) and is part of the Mercury terrain type characterized as “intercrater plains.” These plains have a rough, hummocky texture and a high spatial density of small, superposed craters <15 km in diameter (Trask & Guest 1975; Strom 1977; Schaber & McCauley 1980; Leake 1981); intercrater plains are substantially more rugged in appearance than Mercury’s smooth plains units. Intercrater plains are likely dominantly volcanic in nature, with sustained impact bombardment responsible for their present texture (Whitten et al. 2014; Byrne et al. 2018). The region in which our targeted site lies is among the oldest on Mercury (Denevi et al. 2018b).

The region we selected encompasses several named features, including Liang K’ai, Dowland, and Dostoevskij basins (Figure 6(a)). The region also includes numerous sites where pyroclastic volcanic activity occurred (Byrne et al. 2018; Jozwiak et al. 2018) and several rayed craters, the most prominent of which is Bashō. Smooth plains units are present, although almost all instances are hosted within earlier impact craters and basins (Figure 6(b)).

No images are currently available that show our nominal landing site at the scale of the lander itself, so it is only possible to broadly estimate the morphology of the site at present. Even the highest-resolution images returned by MESSENGER during its low-altitude campaign, which are restricted to the northern hemisphere, are $\sim 2\text{--}3$ m pixel⁻¹, which are insufficient to resolve any features at the scale of the lander such as boulders or similar morphological textures that might pose a hazard to safely landing on the surface. We can, however, draw some inferences from those high-resolution MESSENGER images. The surface of an area of intercrater plains in the northern hemisphere imaged by MESSENGER at ~ 2 m pixel⁻¹ (Figure 6(c)) shows craters from several meters to several hundred meters in diameter; craters at still smaller diameters, as well as similarly sized boulders, are likely present but cannot be resolved in the MESSENGER images. Data from the Mercury Laser Altimeter also do not support characterization of the surface topography or roughness at the lander scale. Even so, the terrain between the larger craters appears relatively level, with little evidence for short-wavelength (i.e., tens of meters), positive-relief topography casting shadows in the scene. Therefore, it is possible, and perhaps likely, that much of Mercury’s intercrater plains between craters hundreds of meters in diameter—and thus resolvable with MESSENGER and BepiColombo data—may be sufficiently level to permit the safe, autonomous landing of a robotic spacecraft. Further quantitative investigations into this topic are highly worthwhile for future Mercury lander mission planning. By way of analog, the Apollo landing sites on the Moon might offer some useful insights. Out of the six landing sites, Mercury’s intercrater plains may most closely resemble the Apollo 17 site—where a small tectonic scarp and several impact-related massifs bracket a relatively smooth landing area (Figure 6(d)).

6.2. BepiColombo Landing Site Characterization

The BepiColombo mission is on its way to Mercury and will start collecting scientific measurements of Mercury as early as 2022. During the six flybys of the planet, only a limited number of instruments will be able to observe Mercury’s surface (Mangano et al. 2021). Improvements to the MESSENGER observations of the landing site will therefore only come from the orbital phase of the mission, planned to begin in 2026. The MPO spacecraft will be positioned to characterize Mercury’s surface at scales and wavelengths better than were possible with MESSENGER. In particular, the Spectrometer and Imaging for MPO BepiColombo Integrated Observatory SYSTEM (SIMBIO-SYS) instrument suite (Flamini et al. 2010; Cremonese et al. 2020) will acquire stereo images to support the creation of targeted digital terrain models (DTMs), high-resolution images, and near-infrared spectra up to 2400 nm, and the Mercury Radiometer and Thermal Infrared Spectrometer (MERTIS) instrument (Hiesinger et al. 2010, 2020) will acquire observations in the infrared domain and will measure the surface temperature.

The MPO spacecraft will have an elliptical orbit that evolves during the mission. Its periapsis will drift rapidly to the south, and the altitude of the spacecraft will decrease. Although the nominal MPO mission is for one Earth year (Benkhoff et al. 2010, 2021), it is expected that by the end of a likely 1-yr extension, the spacecraft argument of periherm will be located at 40°S, with an estimated altitude of 270 km. These orbital properties will position the spacecraft for optimal observations

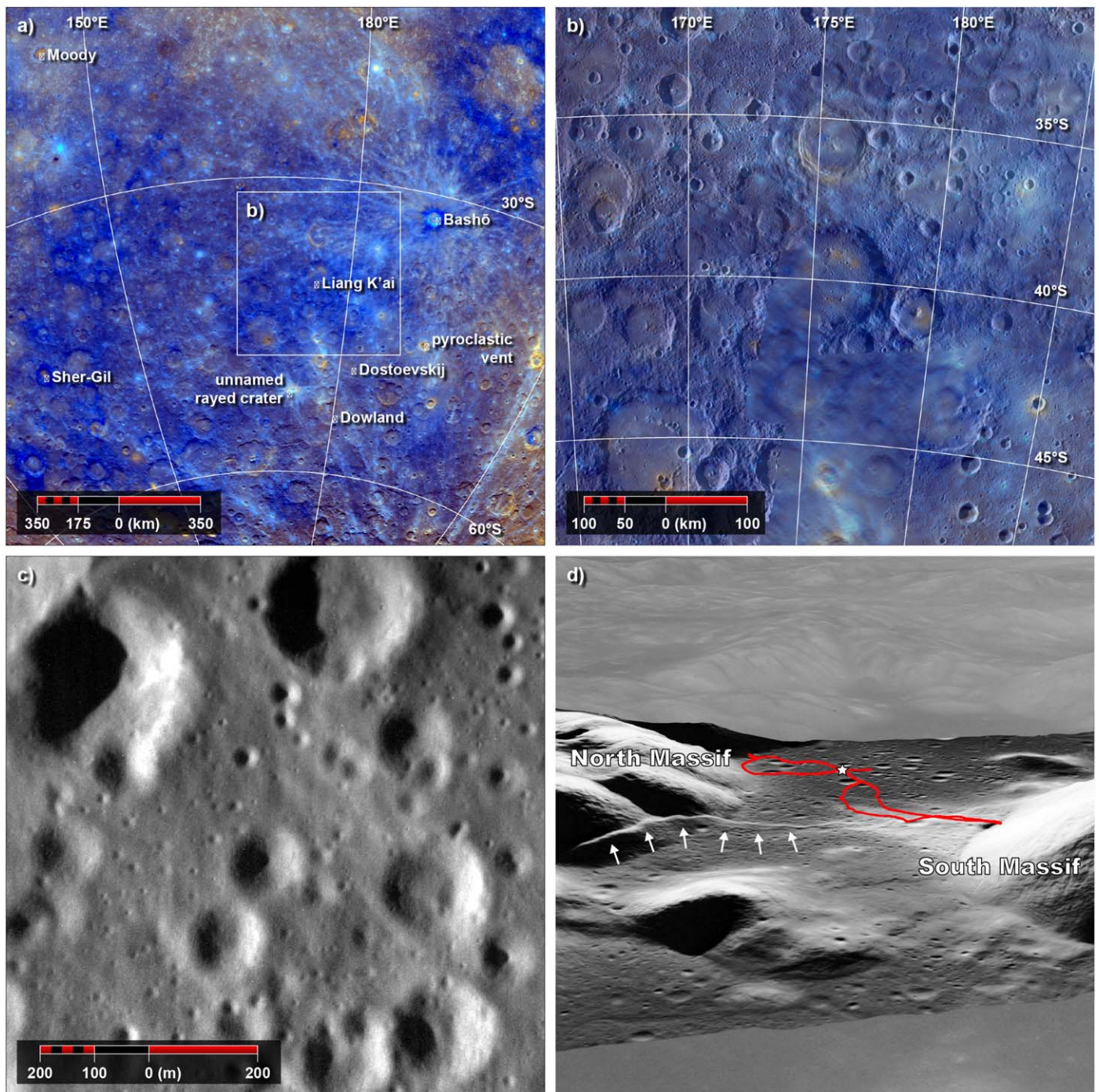


Figure 6. (a) The region of Mercury where our nominal landing site is situated, shown at a view scale of 1:10M and with enhanced color (e.g., Denevi et al. 2018a). Prominent named features are labeled, as is an example rayed crater and pyroclastic vent. Note the expanse of blue LRM throughout the region. The approximate location of panel (b) is marked by the white outline. (b) The same region at a view scale of 1:3M, with the enhanced color global mosaic superposed on the global monochrome mosaic. (c) A MESSENGER MDIS image from that mission’s low-altitude operations phase, showing an exemplar region of the intercrater plains at a resolution of ~ 2 m pixel $^{-1}$. (d) An oblique view of the Taurus-Littrow Valley in Google Earth. The Apollo 17 landing site (star) and traverse path (red line) are indicated. Note the massifs that flank the landing site as well as the Lee Lincoln thrust fault scarp (white arrows) that strikes left–right. The valley width near the center of the image is approximately 7 km.

of the concept study landing site, located at 40°S. In particular, at this phase of the BepiColombo mission,

1. SIMBIO-SYS will acquire high-resolution images of order 2–3 m pixel $^{-1}$ and produce DTMs of resolution ~ 100 m pixel $^{-1}$;
2. MERTIS will obtain unprecedented surface temperature measurements with a resolution of roughly 1 km pixel $^{-1}$;

3. the Mercury Imaging X-Ray Spectrometer (Fraser et al. 2010; Bunce et al. 2020) and Mercury Gamma and Neutron Spectrometer (Mitrofanov et al. 2021) will provide observations of the southern hemisphere at smaller scales than were feasible with MESSENGER; and
4. the BepiColombo Laser Altimeter (Gunderson & Thomas 2010; Thomas et al. 2021) will obtain topographic measurements of the southern hemisphere.

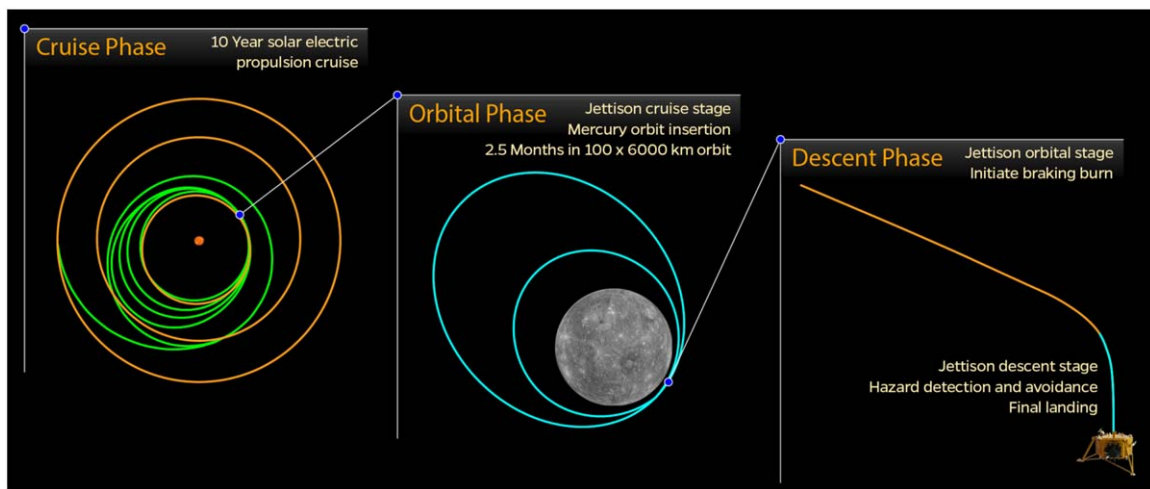


Figure 7. Cruise, orbital, and descent phases in schematic form.

These observations will provide important, new measurements of Mercury’s surface, new insights on Mercury’s southern hemisphere, and new information to characterize the overall scientific setting of the landing site. However, given that any landing site would have to be characterized to a submeter (i.e., lander) scale to fully identify and mitigate potential landing hazards, BepiColombo will not provide the necessary spatial resolution to pinpoint a hazard-free landing site. Dedicated and well-prepared MPO observations during an extended mission may be able to offer measurements that could be useful for characterizing highly localized regions at higher latitudes in Mercury’s southern hemisphere, potentially at a submeter scale to identify hazards. Overall, the risk posed by the uncertainty regarding the Mercury surface at lander scale is not likely to be retired by BepiColombo measurements and will thus remain one of the most substantive challenges facing any landed mission to Mercury.

7. Mission Concept and Science Operations

This section provides a high-level overview of the engineering and technical design resulting from the NASA-funded Mercury Lander concept study, but it focuses largely on the science operations necessary to achieve our stated science goals and objectives. Multiple solutions were considered for each design decision, with final selections primarily motivated by the prioritization of maximized landed mass. Additional detail on the key trade studies and engineering results is given by Kubota et al. (2020) and in the final technical report delivered to NASA (Ernst et al. 2020).

7.1. Mission Concept Overview

This CML-4 (point design) concept addresses the primary challenges of a Mercury Lander mission with a four-stage design that launches on a SpaceX fully expendable Falcon Heavy vehicle. This LV’s increased lift capability is mission enabling. Mass savings are enabled through jettisoning of stages prior to large burns and optimization of propulsion systems for each of the mission’s four phases: cruise, orbit, initial descent, and landing. These phases are illustrated in Figure 7.

The cruise stage minimizes the fuel load required with an SEP system for a low-thrust trajectory to Mercury

Table 2
Nominal Mission Itinerary

| Event | Date |
|--|--------------------|
| Launch | 2035 Mar 23 |
| Earth Flyby (and backup launch) | 2036 Mar 23 |
| Venus Flyby 1 | 2036 Jun 22 |
| Venus Flyby 2 | 2038 Mar 16 |
| Mercury Flyby 1 | 2038 May 19 |
| Mercury Flyby 2 | 2039 Feb 14 |
| Mercury Flyby 3 | 2040 Jan 27 |
| Mercury Flyby 4 | 2041 Jan 18 |
| Mercury Flyby 5 | 2042 Jun 26 |
| Arrival | |
| Jettison Cruise Stage | 2045 Jan 13 |
| Mercury Orbit Insertion (100 km × 6000 km orbit) | |
| Orbital Imaging Campaign | 2045 Feb 11–Mar 22 |
| Lower Apoapsis (100 km × 2000 km orbit) | 2045 Mar 30 |
| Lower Periapsis (20 km × 2000 km orbit) | |
| Jettison Orbital Stage and Sunshades | |
| Deploy Lander Legs | |
| Descent | 2045 Apr 12 |
| Jettison Descent Stage | |
| Landing | |
| Direct-to-Earth Communication Ceases | 2045 May 4 |
| Direct-to-Earth Communication Resumes | 2045 Jun 16 |
| Surface Operations End | 2045 Jul 11 |

(Shannon et al. 2021). A nominal mission timeline selected for this concept study is shown in Table 2; alternate launch and trajectory options exist for a Mercury Lander mission. The Mercury Lander flight system launches from Cape Canaveral on 2035 March 23, with a backup launch period in 2036. The reference trajectory includes one Earth, two Venus, and five Mercury gravity assists during a 10-yr cruise. The four-stage system uses an SEP cruise stage to reach Mercury in 2045

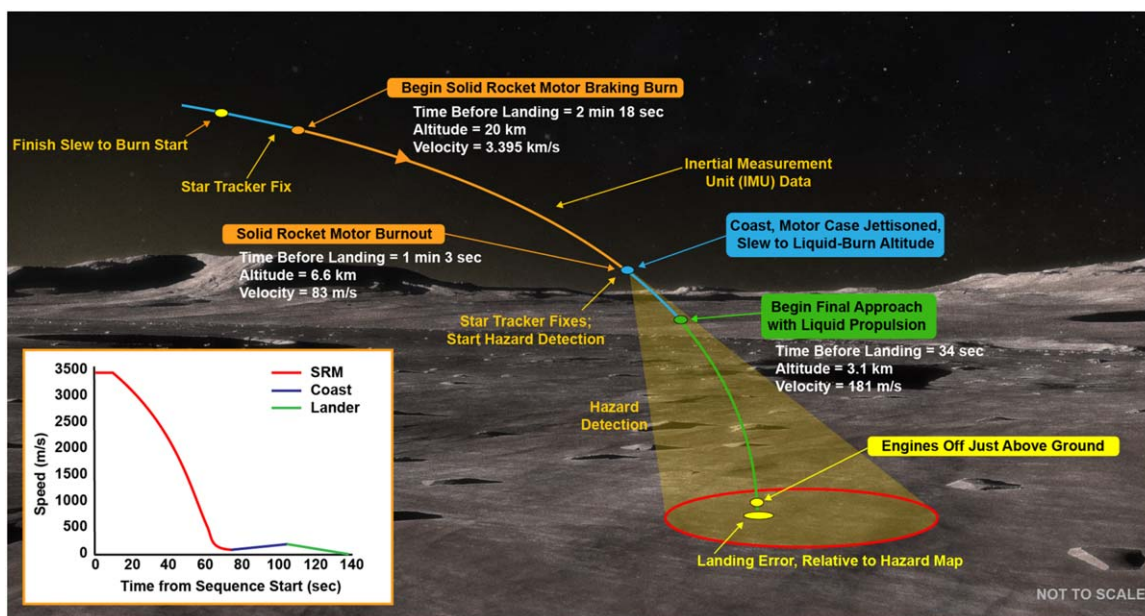


Figure 8. The descent and landing sequence. The sequence begins with a 75 s braking burn executed by the SRM, which reduces most of the orbital energy, decelerating the lander from a high incoming horizontal velocity to a nearly vertical velocity at the end of the burn. Landing uses continuous LIDAR operations post-SRM burn to support hazard detection.

January. The cruise stage is jettisoned after orbit-matching with Mercury.

A chemical propulsion system is chosen for the orbital stage. The Mercury orbit insertion (MOI) burn delivers the remaining three stages to a thermally safe, 100 km \times 6000 km polar parking orbit. The NAC on the orbital stage enables landing site reconnaissance from this orbit, as described in Section 5.5.1. Required landing conditions are met about 2.5 months after MOI. After Mercury's true anomaly position is greater than 130°, an apoherm-lowering maneuver to a 100 km \times 2000 km orbit and a final periherm-lowering maneuver to a 20 km \times 2000 km orbit are executed. These maneuvers are separated by 2 weeks and prepare the vehicle for descent at aphelion with a near-terminator orbit.

The orbital stage is jettisoned prior to initiation of the landing sequence. Mass efficiency through the braking burn is optimized in the descent stage with a STAR 48GXV solid-rocket motor (SRM). The descent stage is jettisoned after SRM burnout, and the lander executes the final soft landing with a bipropellant liquid propulsion system. Landing uses continuous LIDAR operations to support hazard detection and safely deliver the payload to the surface (see Section 7.2).

7.2. Descent and Landing Sequence

The Mercury Lander descent and landing sequence is illustrated in Figure 8. The sequence begins at the 20 km orbit periapsis just over 2 minutes before landing, with a 75 s braking burn executed by the SRM, which negates the bulk of the orbital energy and thus decelerates the vehicle from a 3.395 km s⁻¹ incoming horizontal velocity to an 83 m s⁻¹ nearly vertical velocity at the end of the burn (ΔV of 3.313 km s⁻¹). SRM burnout occurs at \sim 6.6 km altitude, just over 1 minute before landing, and is followed by a 30 s coast arc, jettison of the descent stage, and determination of whether the nominal landing site is sufficiently clear of hazards using a scanning LIDAR and an onboard hazard map generated from collected data. The near-vertical motion achieved at the end of

the braking burn allows for a continuous scan of a single landing area during the coast arc, and an initial landing site is selected at \sim 3.1 km altitude, just over 30 s before landing. Scanning LIDAR performance at this altitude ranges from \sim 0.53 m² pixel⁻¹ over 400 m² to better than 0.1 m² pixel⁻¹ over 540 m², depending on the sampling rate used (10 kHz or 100 kHz, respectively). During the final approach, the guidance system targets the selected site during the liquid burn, while continuing to refine the selection with increased resolution on descent. LIDAR measurements provide translation-state corrections in addition to terrain assessment. Follow-on LIDAR measurements focus on the search area and result in centimeter-level accuracy in hazard detection. This approach builds on the safe landing strategies developed for lunar applications, with the use of multiresolution algorithms for LIDAR processing, and assumes similar terrain and rock size–frequency distribution to that found on the Moon. As for a lunar landing, the final 15 m of descent is performed with the IMU only, to avoid any interference of lofted dust with LIDAR, driving the landing accuracy to a few meters from the selected landing site. The engines cut off just above the ground, and the spacecraft safely delivers the payload to the surface.

7.3. Science Operations

The lander houses the full payload suite, the avionics components that provide command and data handling for the entire flight system, the majority of the telecomm subsystem, a power subsystem including a NextGEN radioisotope thermoelectric generator (RTG) and a small battery, those guidance and control (G&C) sensors required for landing, and a smaller bipropellant propulsion system. Landing occurs at dusk to meet thermal requirements, permitting \sim 30 hr of sunlight for initial observations. The RTG-powered lander continues surface operations through the Mercury night. Direct-to-Earth (DTE) communication is possible for the initial 3 weeks of the landed mission, followed by a 6-week period with no Earth communication. DTE communication resumes for the

remaining 4 weeks of nighttime operations. Thermal conditions exceed lander operating temperatures shortly after sunrise, ending surface operations (see Ernst et al. 2020; Kubota et al. 2020 for technical details). A total of ~ 11 GB of data are returned to Earth. The overall concept of landed operations is depicted graphically in Figure 9 and described below.

7.3.1. Descent Science Observations

DescentCam will commence full-frame imaging at a frequency of 0.5 Hz before the firing of the SRM on the descent stage, pausing during the firing, and resuming during the landing phase after the descent stage burnout and jettison (altitude ~ 7 km, ~ 1 minute prior to landing). The final landing approach with liquid propulsion will begin at an altitude of ~ 3 km, ~ 30 s prior to landing, for which DescentCam will acquire an uninterrupted, nested imaging sequence (for a total of about 60 images at progressively higher resolutions across smaller spatial scales).

The LIDAR is classified as an engineering instrument to aid with landing. Although the primary objective of the LIDAR is not to return science data but rather to enable hazard avoidance and a safe landing on Mercury, the LIDAR data would also provide opportunistic science and will be fully transmitted to Earth. In addition to characterizing the topography of the local landing site, the LIDAR data can provide information regarding shape, surface roughness, and reflectivity of the Mercury surface at a variety of scales, augmenting the science return of the descent camera and other imaging instruments. The LIDAR will operate continuously after the completion of the SRM burn.

7.3.2. Continuously Operating Landed Measurements

Many of the instruments operate nearly continuously throughout the landed mission, including the NMS, IMS, EPS, DD, and the MAC, as well as the MAG (once the boom deploys). The RS investigation also begins, continuing whenever Earth communication is possible. The GRS has a cool-down period after landing and then begins continuous operations approximately 36 hr later. The RTG cools concurrently with the GRS, allowing it to reach full power output before GRS operations begin. The GRS truly operates continuously, whereas, owing to power limitations, all other “continuous” instruments momentarily cease operations during the ~ 1 hr XRD/XRF operations that occur periodically (XRD/XRF operations are described in more detail in Section 7.3.4). The continuous operation of the GRS enables the highest-sensitivity elemental measurements for the mission and minimizes the potential for degradation of the instrument during landed operations. Measurements beyond the required 72 hr will lead to increased precision, as well as insights into regolith density and depth-dependent concentration variations not otherwise possible.

Continuous MAG observations will span local times and heliocentric distances from $\sim 6:00$ pm at aphelion just after landing, to midnight at perihelion some 44 days later, to just after 6:00 am at aphelion at the end of the mission.

Seismic and tidal potential observations will be continuous over the full course of the landed mission. Quake activity can occur at any time throughout the mission, and complete

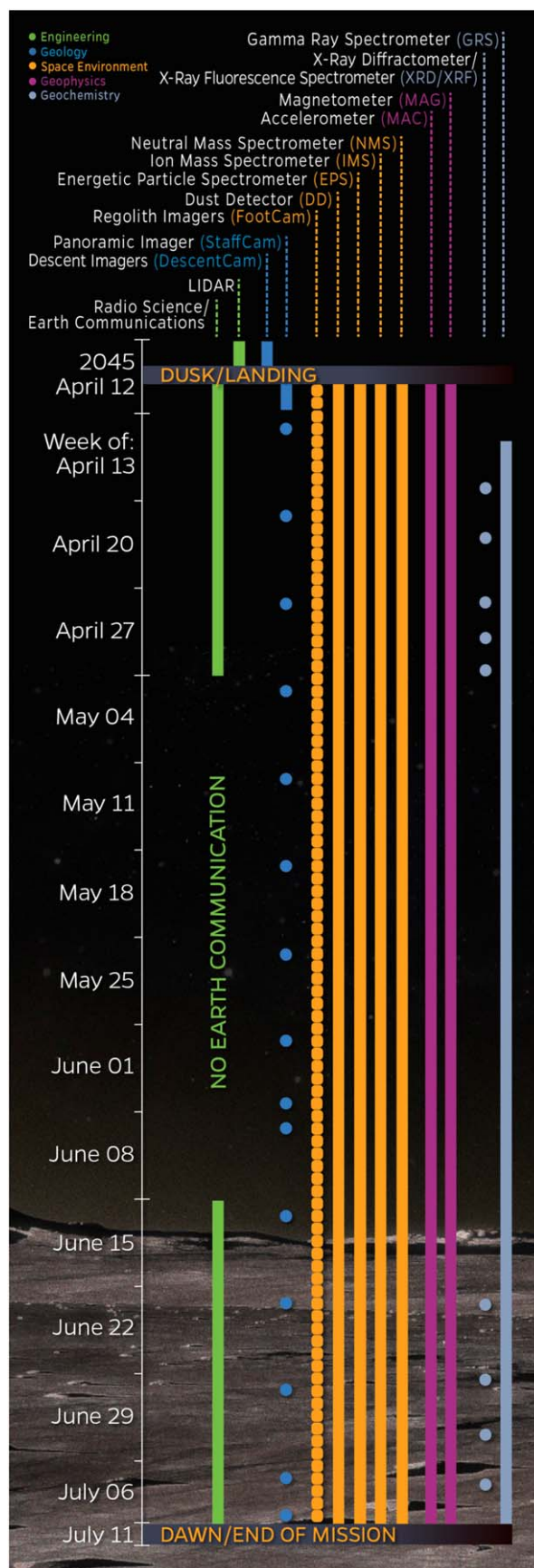


Figure 9. Timeline of landed operations.

monitoring is necessary to quantify the scale and frequency of tectonic activity, and particularly that activity driven by tidal forcing as a result of Mercury's eccentric orbit. Operating as a seismometer, MAC will operate at a 100-sps rate that generates more than 7 GB of data, a considerable fraction of the total available downlink. However, downlinking the full data sets during the periods of direct communication will provide an important baseline on seismicity and thermomechanical behavior of the surface and lander during the post-sunset and pre-dawn periods. Lower-resolution data (1 sps), plus statistical information from the 100-sps data that characterize its variability, will be downlinked upon reconnection from the period without Earth communications. Those data will be analyzed on Earth to prioritize time periods with seismic activity for full-resolution downlinking. Prioritizing 250 hr of data from that period will permit as many as 125 events during that 6-week period to have 2 hr of full-resolution data downlinked for each of those events. This prioritization process can be extended to the second communications period, to further manage both stored and downlinked data volumes.

Mercury's exosphere is continuously produced and maintained at all times, and understanding the time-varying nature of the sources and their relationships to the exosphere requires that as many observations as possible are obtained. The timescales for variations observed in the exosphere and magnetosphere have been as small as minutes to even seconds, and it is impossible to know when the shortest-timescale phenomena are going to be observed. Hence, continuous operations of NMS, IMS, EPS, and DD are planned during the landed mission, within available power constraints. As a balance between the space environment observational needs and those of the rest of the lander, a sampling rate of once every 10 s for all the instruments has been baselined. This rate is enough to capture the shorter timescales relevant to the exosphere, without exceeding or dominating the total data rate of the lander. If data volume limitations arise, the sampling rate could be reduced to once every 100 s for these instruments, but for this mission concept study this lower rate serves as a contingency.

With the combined Mercury space environment landed measurements of the NMS, IMS, EPS, and DD, the source processes for the exosphere can be examined as a truly complete system for the first time. Correlations between the incoming and outgoing material will be established on multiple scales. Because the lander observations will span one Mercury year, the correlations will provide unparalleled insight into the seasonal variations of the source rates, as shown in Figure 10. Should there be unusual circumstances at the surface—perhaps owing to solar energetic particle events, coronal mass ejections, magnetospheric substorms, or a larger meteoroid impact—the lander will provide important knowledge of how those processes change.

7.3.3. Imaging Operations

During the ~30 hr of sunlight from landing at dusk until nightfall, StaffCam and FootCam will capture images and panoramas of the landing site region. StaffCam's initial operation will consist of a set of panoramas of the entire landing site (except in the Sun "keep-out zone") immediately after landing. Imaging obtained with StaffCam and FootCam will allow comparison of more heavily scoured material immediately surrounding the lander with material that is less

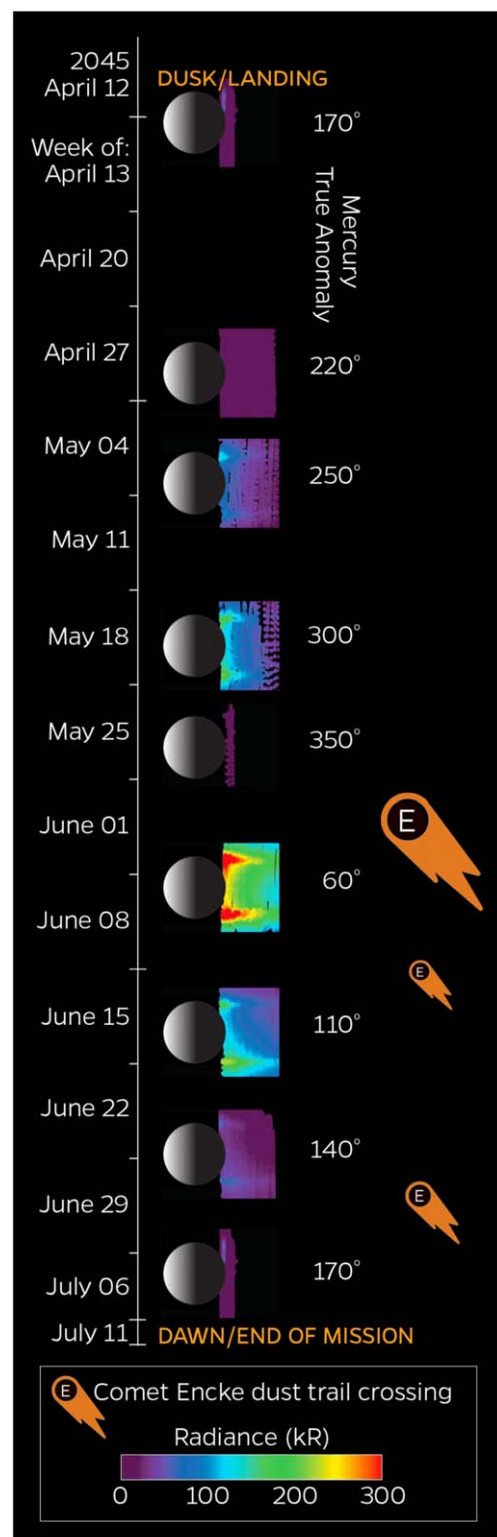


Figure 10. Seasonal coverage from one full Mercury year of landed science operations. The color maps are generated from the Na emission in the tail region of the exosphere observed by MESSENGER and averaged over the orbital phase of the mission (adapted from Cassidy et al. 2016). The size of the comet Encke symbols qualitatively indicates the amount of dust likely to impact Mercury during its approach to the planet when the Mercury Lander is operating there (bigger equals more dust).

disturbed farther afield. A full panorama comprises nine frames to capture the near field and horizon around the lander. Immediately after landing, FootCam will image the landing

Table 3
Landed Operations and Associated Data Volume

| Instrument | NMS | IMS | EPS | DD | GRS | XRD/XRF ^a | MAG | MAC | StaffCam | FootCam | DescentCam | Total |
|-----------------------------------|-------------------|-------------------|-------------------|-------------------|------|---------------------------|-------------------|-------------------|---------------------------|---------|--------------|--------|
| Surface Ops Description | Cont ^b | Cont ^b | Cont ^b | Cont ^b | Cont | Specific Collection Times | Cont ^b | Cont ^b | Specific Collection Times | Daily | Descent Only | |
| Total data volume downlinked (MB) | 228 | 1138 | 228 | 228 | 484 | 93 | 1422 | 4619 ^c | 773 | 1138 | 469 | 10,820 |

Notes.

^a Includes XRD/XRF and PlanetVac data.

^b Continuous except for during XRD/XRF analyses.

^c Only difference between data acquired and data downlinked; MAC acquires 7111 MB of data.

pads to acquire information regarding the mechanical and textural properties of the regolith. Each StaffCam or FootCam image is estimated at 12.5 Mbit (compressed).

LEDs will be used to enable nighttime operations, although the glow from Mercury's Na exosphere may also provide diffuse illumination, particularly when the tail is extended (Figure 10) and total emission intensities rival those of a moderate aurora on Earth. StaffCam acquires a panorama weekly, characterizing the surrounding landscape and the exospheric "glow." Panoramas without LED illumination will also be acquired to search for the possible detection of lofted particles and to characterize the exospheric glow. In particular, on 2045 June 7, which corresponds to Mercury true anomaly of 60°, StaffCam will undertake a dedicated exploratory imaging campaign with multiple panoramas devoted to imaging the Na exosphere, timed to occur during the maximum seasonal radiance (>300 kR), as seen in Figure 10.

FootCam images are acquired daily to monitor for changes, especially before and after PlanetVac operations. FootCam images will be obtained in colors utilizing the LEDs for such imaging. These daily images will provide before-and-after views of each PlanetVac sampler site when that instrument is active. Additionally, FootCam images taken at the 2045 June 7 anticipated peak of the Na exosphere will provide useful insight into illumination conditions of the Mercury soil during this phenomenon.

As the Sun rises at the end of the mission, StaffCam and FootCam acquire multiple images and panoramas, streaming them back to Earth until the lander fails and the transmissions end.

7.3.4. XRD/XRF and PlanetVac Operations

XRD/XRF operations occur in coordination with the operation of PlanetVac, which provides regolith samples to the instrument for analysis. Based on comparison with lunar landings and test data from Earth (e.g., Metzger et al. 2011), the area under the lander will probably experience several centimeters of scouring, depending on the regolith texture and exhaust pressure. For the purpose of sampling, this scouring may allow access to somewhat less space weathered material for mineralogical analysis. Before initial operations begin, images obtained by DescentCam, StaffCam, and FootCam from the sunlit dusk operations will be analyzed by the science team to characterize the regolith properties, such as grain size and morphology and the placement of the PlanetVac samplers on the surface. These images will inform the subsequent operations plans for PlanetVac and XRD/XRF. The baseline plan for this study's landed mission operations

includes eight XRD/XRF analyses, four from each PlanetVac sampler. This plan would allow for both lateral and vertical heterogeneities of the landing site to be assessed, but could also be adjusted based on the specifics of the local landing site.

During the initial 3 weeks of operations and with DTE communication, four distinct PlanetVac samples are analyzed. The baseline plan includes one sample from each of the two PlanetVac samplers within the first 10 days of landed operations. These initial XRD/XRF analyses are planned to last 1 hr each. To assess the efficacy of this measurement time and evaluate the impact of longer analysis time on data quality, several days later these same two samples, which will still be in the XRD/XRF cells, will be reanalyzed for a 4-hr duration. Approximately 2 weeks into the landed mission, both previously acquired samples will be dumped and empty-cell XRD/XRF analyses conducted, to ensure that cells are empty before accepting new samples. During the third week of landed operations, two additional samples will be collected with one of the PlanetVac samplers, with XRD/XRF analysis of each sample followed by subsequent cell dumping and empty-cell analyses conducted a day afterward.

These four initial samples will provide insight into the nature and amount of compositional diversity that may exist between the locations of the two legs, as well as at depth, as PlanetVac excavates deeper into the regolith with each subsequent sample at a given location. The daily FootCam images will provide information on morphological changes occurring with each collection, as well as information regarding depth of sampling.

Owing to the complexities associated with the XRD/XRF instrument and PlanetVac sampling system, no operations are conducted during the period of the landed mission when there is no DTE communication. Once DTE communication is restored for the final 24 days of the mission, the baseline plan includes XRD/XRF analysis of four additional samples; the selection of which PlanetVac(s) to use for these samples will be informed by analysis results of the four initial samples. During the periods of direct-to-Earth communication, all XRD/XRF and PlanetVac data can be fully downlinked to Earth within a few hours of being acquired.

7.3.5. Landed Data Volume

The total data volume acquired for each instrument is given in Table 3. Figure 11 plots the daily data volume acquired, the downlink available for science data, and the loading on the lander's solid-state recorder, assuming *Ka*-band downlink capability and use of a single, 34 m Deep Space Network antenna. The data acquired by all of the instruments are downlinked in full except for data-volume-intensive MAC

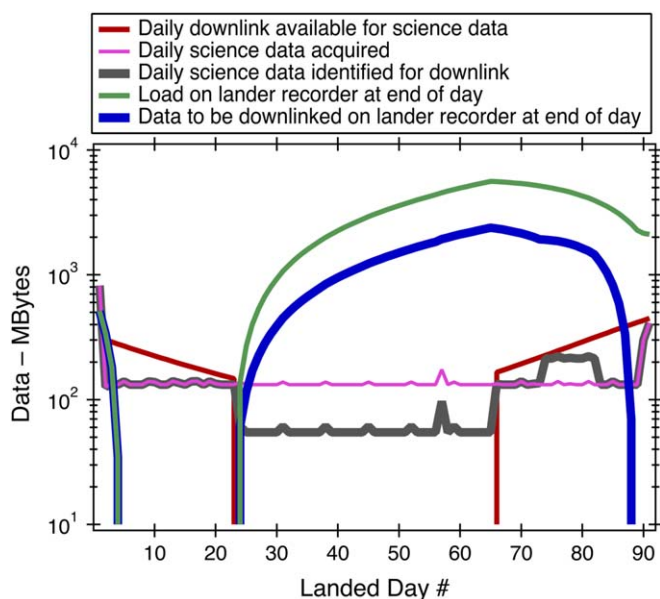


Figure 11. The total landed science data volume and downlink plan, using the 34 m *Ka*-band capability detailed in the text.

observations, which are prioritized as described in Section 7.3.2. In Figure 11, high-frequency MAC data produce the increase around days 75–85 in the “daily science data identified for downlink” line. The peak on that same line at day 59 in Figure 11 is from the dedicated StaffCam exosphere imaging campaign, and smaller weekly peaks are from the weekly StaffCam images. Overall, about 10.8 GB of science data (the nominal data volume) are returned during landed surface operations and are accommodated by the downlink from a single 34 m *Ka*-band antenna. The lander’s recorder is cleared of data identified for downlink a few days in advance of sunrise.

7.3.6. Cruise and Orbital Operations

Instrument operations and observations during the 10-yr cruise phase or the 3 months in Mercury orbit are possible and can provide critical calibration measurements for some instruments. However, landed in situ measurements on the surface of Mercury are required to address the science goals that drive this concept study, so the science operations investigated in the study focused on obtaining the highest-priority landed measurements to achieve the science objectives detailed in Table 1.

7.4. Cost Summary

The cost estimate prepared for Mercury Lander is commensurate with a CML-4 mission concept. A detailed description of the cost estimate is contained within the final technical report delivered to NASA (Ernst et al. 2020).

The Mercury Lander Phase A–F mission cost, including unencumbered reserves of 50% (for Phases A–D, excluding LV costs) and 25% (for Phases E and F, excluding DSN charges), is \$1754.0M in fiscal year 2025 dollars (FY25\$). Excluding LV costs, the Mercury Lander Phase A–F mission cost is \$1508.0M FY25\$ (Figure 12). The Phase A–D mission cost estimate (excluding the LV) is \$1191.9M FY25\$, comparing favorably with recent New Frontiers (NF) missions (Figure 12), as well as to the cost cap prescribed in the New Frontiers 4 AO

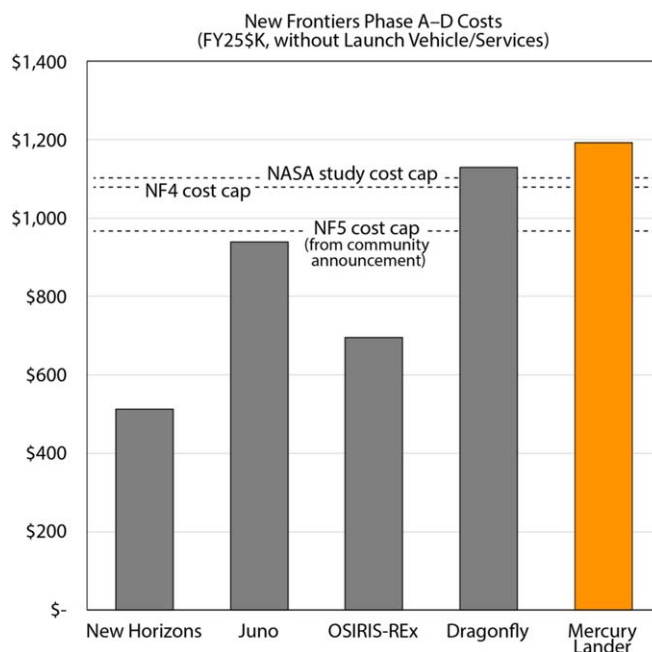


Figure 12. Mission-level cost comparison to New Frontiers missions.

(~\$1.08B FY25\$) and the guideline of \$1.1B FY25\$ provided by NASA for this study. The inflated NF5 cost cap stated in NASA’s Community Announcement in 2020 (~\$970M FY25 \$) is substantially lower than that for NF4 and the NASA study guidelines. Such a lower cost cap might preclude a Mercury Lander mission from contention as a New Frontiers–class mission. With the delay of NF5 to no earlier than 2024 and the anticipated release as of this writing of the 2023–2032 Decadal Survey, the previously stated NF5 cost cap may be reexamined. We are confident that, with further refinement of the design beyond this CML-4 study, a Mercury Lander mission can be developed and shown to be both feasible and compelling as a New Frontiers–class mission in the coming decades.

8. Mission Concept Summary and Conclusions

The Mercury Lander mission concept design presented here demonstrates that groundbreaking science on the innermost planet can be achieved as a New Frontiers–class mission in the coming decades. Scientific and technological advances in the past decade have set the stage for such a mission. The leaps in knowledge driven by MESSENGER were critical for formulating the next-level fundamental science questions to drive Mercury exploration, and we are poised to learn yet more with BepiColombo. But in developing those science questions, it is clear that they can only be answered by in situ measurements from the surface of the planet.

Recent technology advances are mission enabling, including increased LV performance capability, further development and use of SEP, and NextGen RTG development. The Mercury Lander mission concept design described here leverages these scientific and technological advances, achieving one full Mercury year (~88 Earth days) of surface operations with an 11-instrument, high-heritage payload delivered to a landing site within Mercury’s widely distributed LRM. The Mercury Lander mission would provide revolutionary data about the innermost planet, addressing fundamental open science questions about planetary and solar system formation, evolution,

and processes. Given the lengthy cruise time to Mercury, now is the time to prepare for a Mercury lander, to ensure the continued exploration of the innermost planet after BepiColombo.

The Mercury Lander study was supported by the NASA Planetary Mission Concept Study Program grant 80NSSC20 K0122 to C.M.E. We thank the APL-based engineering and report development teams for their hard work and dedication to this study, especially under trying circumstances. We thank Dean Bergman, David Blake, Thomas Bristow, Bob Downs, David Lawrence, Ralph Lorenz, Francis McCubbin, Dick Morris, Philippe Sarrazin, and Kris Zacny for their helpful discussions on the instruments considered for the payload. We also thank Larry Nittler and Bernard Charlier for their thoughtful reviews and Faith Vilas for editorial handling.

ORCID iDs

Carolyn M. Ernst  <https://orcid.org/0000-0002-9434-7886>
 Nancy L. Chabot  <https://orcid.org/0000-0001-8628-3176>
 Rachel L. Klima  <https://orcid.org/0000-0002-9151-6429>
 Paul K. Byrne  <https://orcid.org/0000-0002-5644-7069>
 Steven A. Hauck, II  <https://orcid.org/0000-0001-8245-146X>
 Kathleen E. Vander Kaaden  <https://orcid.org/0000-0001-9592-588X>
 Ronald J. Vervack, Jr.  <https://orcid.org/0000-0002-8227-9564>
 Sébastien Besse  <https://orcid.org/0000-0002-1052-5439>
 David T. Blewett  <https://orcid.org/0000-0002-9241-6358>
 Brett W. Denevi  <https://orcid.org/0000-0001-7837-6663>
 Sander Goossens  <https://orcid.org/0000-0002-7707-1128>
 Noam R. Izenberg  <https://orcid.org/0000-0003-1629-6478>
 Catherine L. Johnson  <https://orcid.org/0000-0001-6084-0149>
 Haje Korth  <https://orcid.org/0000-0001-7394-7439>
 Ralph L. McNutt, Jr.  <https://orcid.org/0000-0002-4722-9166>
 Patrick N. Peplowski  <https://orcid.org/0000-0001-7154-8143>
 Jim M. Raines  <https://orcid.org/0000-0001-5956-9523>
 Elizabeth B. Rampe  <https://orcid.org/0000-0002-6999-0028>
 Shoshana Z. Weider  <https://orcid.org/0000-0003-1034-909X>

References

- Anderson, B. J., Acuña, M. H., Lohr, D. A., et al. 2007, *SSRv*, 131, 417
 Anderson, B. J., Johnson, C. L., Korth, H., et al. 2011, *Sci*, 333, 1859
 Andrews, G. B., Zurbuchen, T. H., Mauk, B. H., et al. 2007, *SSRv*, 131, 523
 Asmar, S. W., Armstrong, J. W., Iess, L., & Tortora, P. 2005, *RaSc*, 40, RS2001
 Asmar, S. W., Lazio, J., Atkinson, D. H., et al. 2019, *RaSc*, 54, 365
 Baker, D. N., Dewey, R. M., Lawrence, D. J., et al. 2016, *JGRA*, 121, 2171
 Bandfield, D. A., Rodriguez-Manfredi, J. A., Russell, C. T., et al. 2019, *SSRv*, 215, 4
 Barclay, T., Rowe, J. F., Lissauer, J. J., et al. 2013, *Natur*, 494, 452
 Bell, J. F., Squyres, S. W., Herkenhoff, K. E., et al. 2003, *JGRE*, 108, 8063
 Benkhoff, J., Murakami, G., Baumjohann, W., et al. 2021, *SSRv*, 217, 90
 Benkhoff, J., van Casteren, J., Hayakawa, H., et al. 2010, *P&SS*, 58, 2
 Bennett, C. J., Pirim, C., & Orlando, T. M. 2013, *ChRv*, 113, 9086
 Benz, W., Anic, A., Horner, J., & Whitby, J. A. 2007, *SSRv*, 132, 189
 Bertotti, B., Comoretto, G., & Iess, L. 1993, *A&A*, 269, 608
 Bida, T. A., & Killen, R. M. 2017, *Icar*, 289, 227
 Bish, D. L., & Howard, S. A. 1988, *JApCr*, 21, 86
 Blake, D., Vaniman, D., Achilles, C., et al. 2012, *SSRv*, 170, 341
 Blake, D. F., Sarrazin, P., Bristow, T. F., et al. 2019, *LPSC*, 50, 1468
 Blewett, D. T., Chabot, N. L., Denevi, B. W., et al. 2011, *Sci*, 333, 1856
 Blewett, D. T., Ernst, C. M., Murchie, S. L., & Vilas, F. 2018, in *Mercury: The View After Messenger*, ed. S. C. Solomon et al. (Cambridge: Cambridge Univ. Press), 324
 Blewett, D. T., Stadermann, A. C., Susorney, H. C., et al. 2016, *JGRE*, 121, 1798
 Blewett, D. T., Vaughan, W. M., Xiao, Z., et al. 2013, *JGRE*, 118, 1013
 Broadfoot, A. L., Shemansky, D. E., & Kumar, S. 1976, *GeoRL*, 3, 577
 Brown, S. M., & Elkins-Tanton, L. T. 2009, *E&PSL*, 286, 446
 Bunce, E. J., Martindale, A., Lindsay, S., et al. 2020, *SSRv*, 216, 126
 Burger, M. H., Killen, R. M., McClintock, W. E., et al. 2012, *JGRE*, 117, E00L11
 Burger, M. H., Killen, R. M., McClintock, W. E., et al. 2014, *Icar*, 238, 51
 Byrne, P. K., Klimczak, C., Şengör, A. M. C., et al. 2014, *NatGe*, 7, 301
 Byrne, P. K., Whitten, J. L., Klimczak, C., McCubbin, F. M., & Ostrach, L. R. 2018, in *Mercury: The View After Messenger*, ed. S. C. Solomon et al. (Cambridge: Cambridge Univ. Press), 287
 Cao, H., Aumou, J. M., Wicht, J., et al. 2014, *GeoRL*, 41, 4127
 Cassidy, T. A., McClintock, W. E., Killen, R. M., et al. 2016, *GeoRL*, 43, 11,121
 Cassidy, T. A., Merkel, A. W., Burger, M. H., et al. 2015, *Icar*, 248, 547
 Chabot, N. L., Lawrence, D. J., Neumann, G. A., Feldman, W. C., & Paige, D. A. 2018, in *Mercury: The View After Messenger*, ed. S. C. Solomon et al. (Cambridge: Cambridge Univ. Press), 346
 Charlier, B., Grove, T. L., & Zuber, M. T. 2013, *E&PSL*, 363, 50
 Chipera, S. J., & Bish, D. L. 2002, *JApCr*, 35, 744
 Christensen, U. R. 2006, *Natur*, 444, 1056
 Christou, A. A., Killen, R. M., & Burger, M. H. 2015, *GeoRL*, 42, 7311
 Cremonese, G., Capaccioni, F., Capria, M. T., et al. 2020, *SSRv*, 216, 75
 Delcourt, D. C., Grimald, S., Leblanc, F., et al. 2003, *AnGeo*, 21, 1723
 Denevi, B. W., Chabot, N. L., Murchie, S. L., et al. 2018a, *SSRv*, 214, 2
 Denevi, B. W., Ernst, C. M., Prockter, L. M., & Robinson, M. S. 2018b, in *Mercury: The View After Messenger*, ed. S. C. Solomon et al. (Cambridge: Cambridge Univ. Press), 144
 Dewey, R. M., Raines, J. M., Sun, W., Slavin, J. A., & Poh, G. 2018, *GeoRL*, 45, 10,110
 Dewey, R. M., Slavin, J. A., Raines, J. M., Baker, D. N., & Lawrence, D. J. 2017, *JGRA*, 122, 12,170
 Domingue, D. L., Chapman, C. R., Killen, R. M., et al. 2014, *SSRv*, 181, 121
 Dumberry, M. 2011, *GeoRL*, 38, L16202
 Dumberry, M., Rivoldini, A., Van Hoolst, T., & Yseboodt, M. 2013, *Icar*, 225, 62
 Ebel, D. S., & Stewart, S. T. 2018, in *Mercury: The View After Messenger*, ed. S. C. Solomon et al. (Cambridge: Cambridge Univ. Press), 497
 Eppes, M.-C., Willis, A., Molaro, J., Abernathy, S., & Zhou, B. 2015, *NatCo*, 6, 6712
 Ernst, C. M., Kubota, S., Chabot, N., et al. 2020, Report submitted to NASA and the Planetary Science and Astrobiology Decadal Survey, arXiv:2107.06795
 Evans, L. G., Peplowski, P. N., McCubbin, F. M., et al. 2015, *Icar*, 257, 417
 Evans, L. G., Peplowski, P. N., Rhoades, E. A., et al. 2012, *JGRE*, 117, E00L07
 Flamini, E., Capaccioni, F., Colangeli, L., et al. 2010, *P&SS*, 58, 125
 Folkner, W., Yoder, C., Yuan, D., Standish, E., & Preston, R. 1997, *Sci*, 278, 1749
 Folkner, W. M., Dehant, V., Le Maistre, S., et al. 2018, *SSRv*, 214, 100
 Fraser, G. W., Carpenter, J. D., Rothery, D. A., et al. 2010, *P&SS*, 58, 79
 Genova, A., Goossens, S., Mazarico, E., et al. 2019, *GeoRL*, 46, 3625
 Genova, A., Hussmann, H., Van Hoolst, T., et al. 2021, *SSRv*, 217, 31
 Gershman, D. J., Slavin, J. A., Raines, J. M., et al. 2014, *GeoRL*, 41, 5740
 Giardini, D., Lognonné, P., Banerdt, W. B., et al. 2020, *NatGe*, 13, 205
 Goldsten, J. O., Rhodes, E. A., Boynton, W. V., et al. 2007, *SSRv*, 131, 339
 Grotzinger, J. P., Crisp, J., Vasavada, A. R., et al. 2012, *SSRv*, 170, 5
 Gunderson, K., & Thomas, N. 2010, *P&SS*, 58, 309
 Hapke, B. 2001, *JGRE*, 106, 10039
 Hauck, S. A., II, Dombard, A. J., Phillips, R. J., & Solomon, S. C. 2004, *E&PSL*, 222, 713
 Hauck, S. A., II, Grott, M., Byrne, P. K., et al. 2018, in *Mercury: The View After Messenger*, ed. S. C. Solomon et al. (Cambridge: Cambridge Univ. Press), 516
 Hauck, S. A., II, & Johnson, C. L. 2019, *Elements Magazine*, 15, 21
 Hauck, S. A., II, Margot, J.-L., Solomon, S. C., et al. 2013, *JGRE*, 118, 1204
 Hauck, S. A., II, Eng, D. A., Tahu, G. J., et al. 2010, *Mercury Lander Mission Concept Study*, https://sites.nationalacademies.org/cs/groups/ssbsite/documents/webpage/ssb_059301.pdf
 Head, J. W., Chapman, C. R., Strom, R. G., et al. 2011, *Sci*, 333, 1853
 Hiesinger, H., Helbert, J., & MERTIS Co-I Team 2010, *P&SS*, 58, 144
 Hiesinger, H., Helbert, J., Alemanno, G., et al. 2020, *SSRv*, 216, 110
 Ho, G. C., Krimigis, S. M., Gold, R. E., et al. 2012, *JGRA*, 117, A00M04
 Ho, G. C., Starr, R. D., Gold, R. E., et al. 2011, *P&SS*, 59, 2016
 Ho, G. C., Starr, R. D., Krimigis, S. M., et al. 2016, *GeoRL*, 43, 550
 Hood, L. L. 2016, *JGRE*, 121, 1016
 Horányi, M., Hoxie, V., James, D., et al. 2008, *SSRv*, 140, 387

- Iess, L., Di Benedetto, M., Marabucci, M., & Racioppa, P. 2012, in 23rd Int. Symp. on Space Flight Dynamics (Pasadena, CA: ISSFD), https://issfd.org/ISSFD_2012/ISSFD23_OD1_6.pdf
- Iess, L., Folkner, W. M., Durante, D., et al. 2018, *Natur*, **555**, 220
- Jacobson, R. A., Konopliv, A. S., Park, R. S., & Folkner, W. M. 2018, *P&SS*, **152**, 107
- Johnson, C. L., Anderson, B. J., Korth, H., et al. 2018, in *Mercury: The View After Messenger*, ed. S. C. Solomon et al. (Cambridge: Cambridge Univ. Press), 114
- Johnson, C. L., Mittelholz, A., Langlais, B., et al. 2020, *NatGe*, **13**, 199
- Johnson, C. L., Phillips, R. J., Purucker, M. E., et al. 2015, *Sci*, **348**, 892
- Johnson, C. L., Philpott, L. C., Anderson, B. J., et al. 2016, *GeoRL*, **43**, 2436
- Jozwiak, L. M., Head, J. W., & Wilson, L. 2018, *Icar*, **302**, 191
- Katsura, T., Shimizu, H., Momoki, N., & Toh, H. 2021, *Icar*, **354**, 114112
- Kerber, L., Head, J. W., Blewett, D. T., et al. 2011, *P&SS*, **59**, 1895
- Kerber, L., Head, J. W., Solomon, S. C., et al. 2009, *E&PSL*, **285**, 263
- Killen, R. M., Bida, T. A., & Morgan, T. H. 2005, *Icar*, **173**, 300
- Killen, R. M., Burger, M. H., Vervack, R. J., Jr., & Cassidy, T. A. 2018, in *Mercury: The View After Messenger*, ed. S. C. Solomon et al. (Cambridge: Cambridge Univ. Press), 407
- Killen, R. M., & Hahn, J. M. 2015, *Icar*, **250**, 230
- Klima, R. L., Denevi, B. W., Ernst, C. M., Murchie, S. L., & Peplowski, P. N. 2018, *GeoRL*, **45**, 2945
- Kobayashi, M., Shibata, H., Nogami, K., et al. 2020, *SSRv*, **216**, 144
- Koning, A., & Dumberry, M. 2013, *Icar*, **223**, 40
- Konopliv, A. S., Asmar, S. W., Folkner, W. M., et al. 2011, *Icar*, **211**, 401
- Konopliv, A. S., Yoder, C. F., Standish, E. M., Yuan, D. N., & Sjogren, W. L. 2006, *Icar*, **182**, 23
- Kubota, S., Rogers, G., Ernst, C. M., et al. 2020, in 2020 IEEE Aerospace Conf. (Piscataway, NJ: IEEE), 1
- Kuchynka, P., Folkner, W. M., Konopliv, A. S., et al. 2014, *Icar*, **229**, 340
- Lawrence, D. J., Anderson, B. J., Baker, D. N., et al. 2015, *JGRA*, **120**, 2851
- Lawrence, D. J., Burks, M., Cully, M., et al. 2019a, *LPSC*, **50**, 1554
- Lawrence, D. J., Feldman, W. C., Goldsten, J. O., et al. 2013, *Sci*, **339**, 292
- Lawrence, D. J., Peplowski, P. N., Beck, A. W., et al. 2019b, *E&SS*, **6**, 2605
- Leake, M. A. 1981, PhD thesis, Univ. Arizona, <http://hdl.handle.net/10150/290571>
- Lewis, K. W., Peters, S., Gonter, K., et al. 2019, *Sci*, **363**, 535
- Lindsay, S. T., James, M. K., Buncea, E. J., et al. 2016, *P&SS*, **125**, 72
- Lognonné, P., Banerdt, W. B., Giardini, D., et al. 2019, *SSRv*, **215**, 12
- Lognonné, P., Banerdt, W. B., Pike, W. T., et al. 2020, *NatGe*, **13**, 213
- Mangano, V., Dósa, M., Fränz, M., et al. 2021, *SSRv*, **217**, 23
- Mann, I., Kimura, H., Biesecker, D. A., et al. 2004, *SSRv*, **110**, 269
- Margot, J.-L., Hauck, S. A., II, Mazarico, E., Padovan, S., & Peale, S. J. 2018, in *Mercury: The View After Messenger*, ed. S. C. Solomon et al. (Cambridge: Cambridge Univ. Press), 85
- Margot, J.-L., Peale, S. J., Jurgens, R. F., Slade, M. A., & Holin, I. V. 2007, *Sci*, **316**, 710
- Margot, J.-L., Peale, S. J., Solomon, S. C., et al. 2012, *JGRE*, **117**, E00L09
- McCoy, T. J., Peplowski, P. N., McCubbin, F. M., & Weider, S. Z. 2018, in *Mercury: The View After Messenger*, ed. S. C. Solomon et al. (Cambridge: Cambridge Univ. Press), 176
- McCubbin, F. M., Riner, M. A., Vander Kaaden, K. E., & Burkemper, L. K. 2012, *GeoRL*, **39**, L09202
- McCubbin, F. M., Vander Kaaden, K. E., Peplowski, P. N., et al. 2017, *JGRE*, **122**, 2053
- McNutt, R. L., Livi, S. A., Gurnee, R. S., et al. 2008, *SSRv*, **140**, 315
- Mendillo, M., Warell, J., Limaye, S. S., et al. 2001, *P&SS*, **49**, 1501
- Merkel, A. W., Cassidy, T. A., Vervack, R. J., Jr., et al. 2017, *Icar*, **281**, 46
- Merkel, A. W., Vervack, R. J., Jr., Killen, R. M., et al. 2018, *GeoRL*, **45**, 6790
- Metzger, P. T., Smith, J., & Lane, J. E. 2011, *JGRE*, **116**, E06005
- Milillo, A., Fujimoto, M., Murakami, G., et al. 2020, *SSRv*, **216**, 93
- Mitrofanov, I. G., Kozyrev, A. S., Lisov, D. I., et al. 2021, *SSRv*, **217**, 67
- Morrison, S. M., Downs, R. T., Blake, D. F., et al. 2018, *AmMin*, **103**, 848
- Murakami, G., Hayakawa, H., Ogawa, H., et al. 2020, *SSRv*, **216**, 113
- Murchie, S. L., Klima, R. L., Denevi, B. W., et al. 2015, *Icar*, **254**, 287
- Murray, B. C., Belton, M. J. S., Danielson, G. E., et al. 1974, *Sci*, **185**, 169
- Murray, B. C., Strom, R. G., Trask, N. J., et al. 1975, *JGR*, **80**, 2508
- Namur, O., & Charlier, B. 2017, *NatGe*, **10**, 9
- Namur, O., Charlier, B., Holtz, F., Cartier, C., & McCammon, C. 2016, *E&PSL*, **448**, 102
- National Research Council 2011, *Vision and Voyages for Planetary Science in the Decade 2013–2022* (Washington, DC: The National Academies Press)
- Ness, N. F., Behannon, K. W., Lepping, R. P., & Whang, Y. C. 1975, *Natur*, **255**, 204
- Ness, N. F., Behannon, K. W., Lepping, R. P., Whang, Y. C., & Schatten, K. H. 1974, *Sci*, **185**, 151
- Neumann, G. A., Cavanaugh, J. F., Sun, X., et al. 2013, *Sci*, **339**, 296
- Nittler, L. R., Chabot, N. L., Grove, T. L., & Peplowski, P. N. 2018, in *Mercury: The View After Messenger*, ed. S. C. Solomon (Cambridge: Cambridge Univ. Press), 30
- Nittler, L. R., Frank, E. A., Weider, S. Z., et al. 2020, *Icar*, **345**, 113716
- Nittler, L. R., Starr, R. D., Weider, S. Z., et al. 2011, *Sci*, **333**, 1847
- Nogami, K., Fujii, M., Ohashi, H., et al. 2010, *P&SS*, **58**, 108
- Orsini, S., Livi, S. A., Lichtenegger, H., et al. 2021, *SSRv*, **217**, 11
- Padovan, S., Margot, J.-L., Hauck, S. A., II, Moore, W. B., & Solomon, S. C. 2014, *JGRE*, **119**, 850
- Paige, D. A., Siegler, M. A., Harmon, J. K., et al. 2013, *Sci*, **339**, 300
- Peale, S. J. 1976, *Natur*, **262**, 765
- Peale, S. J. 2005, *Icar*, **178**, 4
- Peplowski, P. N. 2016, *P&SS*, **134**, 36
- Peplowski, P. N., Bazell, D., Evans, L. G., et al. 2015, *M&PS*, **50**, 353
- Peplowski, P. N., Evans, L. G., Hauck, S. A., II, et al. 2011, *Sci*, **333**, 1850
- Peplowski, P. N., Evans, L. G., Stockstill-Cahill, K. R., et al. 2014, *Icar*, **228**, 86
- Peplowski, P. N., Klima, R. L., Lawrence, D. J., et al. 2016, *NatGe*, **9**, 273
- Peplowski, P. N., Lawrence, D. J., Rhodes, E. A., et al. 2012, *JGRE*, **117**, E00L04
- Pieters, C. M., & Noble, S. K. 2016, *JGRE*, **121**, 1865
- Pike, W., Standley, I. M., Calcutt, S. B., & Mukherjee, A. G. 2018, in 2018 IEEE Micro Electro Mechanical Systems (MEMS) (Piscataway, NJ: IEEE), 113
- Pokorný, P., Sarantos, M., & Janches, D. 2018, *ApJ*, **863**, 31
- Raines, J. M., Gershman, D. J., Slavin, J. A., et al. 2014, *JGRA*, **119**, 6587
- Raines, J. M., Gershman, D. J., Zurbuchen, T. H., et al. 2013, *JGRA*, **118**, 1604
- Rampe, E. B., Blake, D. F., Bristow, T. F., et al. 2020, *ChEG*, **80**, 125605
- Rivera-Valentin, E. G., & Barr, A. C. 2014, *E&PSL*, **391**, 234
- Rivoldini, A., & Van Hoolst, T. 2013, *E&PSL*, **377**, 62
- Robinson, M. S., Brylow, S. M., Tschimmel, M., et al. 2010, *SSRv*, **150**, 81
- Rothery, D. A., Massironi, M., Alemanno, G., et al. 2020, *SSRv*, **216**, 66
- Schaber, G. G., & McCauley, J. F. 1980, U.S.G.S. Investigations Map Series (Denver, CO: USGS), 1199
- Schubert, G., Ross, M. N., Stevenson, D. J., & Spohn, T. 1988, in *Mercury*, ed. F. Vilas et al. (Tucson, AZ: Univ. Arizona Press), 429
- Shannon, J. L., Atchison, J. A., Villac, B. F., Rogers, G., & Ozimek, M. T. 2021, *JAnSc*, **68**, 995
- Siegfried, R. W., II, & Solomon, S. C. 1974, *Icar*, **23**, 192
- Slavin, J. A., Acuña, M. H., Anderson, B. J., et al. 2008, *Sci*, **321**, 85
- Slavin, J. A., Anderson, B. J., Zurbuchen, T. H., et al. 2009, *GeoRL*, **36**, L02101
- Slavin, J. A., DiBraccio, G. A., Gershman, D. J., et al. 2014, *JGRA*, **119**, 8087
- Smith, D. E., Zuber, M. T., Lemoine, F. G., et al. 2012, *Sci*, **336**, 214
- Smith, P. H., Tamppari, L. K., Arvidson, R. E., et al. 2009, *Sci*, **325**, 58
- Solomon, S. C. 1976, *Icar*, **28**, 509
- Solomon, S. C., McNutt, R. L., Jr., Gold, R. E., et al. 2001, *P&SS*, **49**, 1445
- Sprague, A. L., Deutsch, L. K., Hora, J., et al. 2000, *Icar*, **147**, 421
- Squires, S. W., Arvidson, R. E., Bollen, D., et al. 2006, *JGRE*, **111**, E12S12
- Stähler, S. C., Kedar, S., van Driel, M., et al. 2017, in 19th EGU General Assembly, Vienna, Austria, 5626
- Stark, A., Oberst, J., Preusker, F., et al. 2015, *GeoRL*, **42**, 7881
- Starr, R. D., Schriver, D., Nittler, L. R., et al. 2012, *JGRE*, **117**, E00L02
- Steinbrügge, G., Padovan, S., Hussmann, H., et al. 2018, *JGRE*, **123**, 2760
- Stockstill-Cahill, K. R., McCoy, T. J., Nittler, L. R., Weider, S. Z., & Hauck, S. A., II 2012, *JGRE*, **117**, E00L15
- Strom, R. G. 1977, *PEPI*, **15**, 156
- Thomas, N., Hussmann, H., Spohn, T., et al. 2021, *SSRv*, **217**, 25
- Thomas, R. J., Rothery, D. A., Conway, S. J., & Anand, M. 2014, *Icar*, **229**, 221
- Thomas, R. J., Rothery, D. A., Conway, S. J., & Anand, M. 2015, *E&PSL*, **431**, 164
- Tian, Z., Zuber, M. T., & Stanley, S. 2015, *Icar*, **260**, 263
- Tosi, N., Grott, M., Plesa, A. C., & Breuer, D. 2013, *JGRE*, **118**, 2474
- Trask, N. J., & Guest, J. E. 1975, *JGR*, **80**, 2461
- Turtle, E. P., Trainer, M. G., Barnes, J. W., et al. 2019, *LPSC*, **50**, 2888
- Van Hoolst, T., Rivoldini, A., Baland, R.-M., & Yseboodt, M. 2012, *E&PSL*, **333**, 83
- Vander Kaaden, K. E., & McCubbin, F. M. 2015, *JGRE*, **120**, 195
- Vander Kaaden, K. E., & McCubbin, F. M. 2016, *GeCoA*, **173**, 246
- Vander Kaaden, K. E., McCubbin, F. M., Byrne, P. K., et al. 2019, *SSRv*, **215**, 49

- Vander Kaaden, K. E., McCubbin, F. M., Nittler, L. R., et al. 2017, *Icar*, [285](#), [155](#)
- Veasey, M., & Dumberry, M. 2011, *Icar*, [214](#), [265](#)
- Vervack, R. J., Jr., Killen, R. M., & McClintock, W. E. 2016, *GeoRL*, [43](#), [11](#),[545](#)
- Wardinski, I., Langlais, B., & Thébault, E. 2019, *JGRE*, [124](#), [2178](#)
- Watters, T. R., Daud, K., Banks, M. E., et al. 2016, *NatGe*, [9](#), [743](#)
- Weider, S. Z., Nittler, L. R., Murchie, S. L., et al. 2016, *GeoRL*, [43](#), [3653](#)
- Weider, S. Z., Nittler, L. R., Starr, R. D., et al. 2015, *E&PSL*, [416](#), [109](#)
- Weider, S. Z., Nittler, L. R., Starr, R. D., Crapster-Pregont, E. J., & Solomon, S. C. 2014, *Icar*, [235](#), [170](#)
- Whitten, J. L., Head, J. W., Denevi, B. W., & Solomon, S. C. 2014, *Icar*, [241](#), [97](#)
- Williams, J. G., & Boggs, D. H. 2015, *JGRE*, [120](#), [689](#)
- Winslow, R. M., Johnson, C. L., Anderson, B. J., et al. 2014, *GeoRL*, [41](#), [4463](#)
- Yoder, C., Konopliv, A., Yuan, D., Standish, E., & Folkner, W. 2003, *Sci*, [300](#), [299](#)
- Yoder, C. F., & Standish, E. M. 1997, *JGRE*, [102](#), [4065](#)
- Zacny, K., Betts, B., Hedlund, M., et al. 2014, in 2014 IEEE Aerospace Conf. (Piscataway, NJ), 1
- Zacny, K., Craft, K., Hedlund, M., et al. 2010, in AIAA Space 2010 Conf. & Exposition (Reston, VA: AIAA), 1
- Zacny, K., Hedlund, M., Herman, J., et al. 2012, in 2012 IEEE Aerospace Conf. (Piscataway, NJ: IEEE), 1
- Zacny, K., Thomas, L., Paulsen, G., et al. 2020, in 2020 IEEE Aerospace Conf. (Piscataway, NJ: IEEE), 1
- Zolotov, M. Y., Sprague, A. L., Hauck, S. A., II, et al. 2013, *JGRE*, [118](#), [138](#)
- Zurbuchen, T. H., Raines, J. M., Gloeckler, G., et al. 2008, *Sci*, [321](#), [90](#)
- Zurbuchen, T. H., Raines, J. M., Slavin, J. A., et al. 2011, *Sci*, [333](#), [1862](#)